Cabibbo-Suppressed Decays of the D^+ Meson

DISSERTATION

Presented in Partial Fulfillment of the Requirements for

the Degree Doctor of Philosophy in the

Graduate School of The Ohio State University

By

Chul Gwon

* * * * *

The Ohio State University

2003

Dissertation Committee:

Klaus Honscheid, Adviser

Richard Kass

Stephen Pinsky

Charles Pennington

Warren Sinnott

Approved by

Adviser
Department of Physics

ABSTRACT

Using 13.7 fb^{-1} from the CLEO II and II.V detectors, we measure the branching ratios for two singly Cabibbo-suppressed decay modes: $\mathrm{BR}(D \to \pi^+\pi^0) = (1.3 \pm 0.2) \times 10^{-3}$ and $\mathrm{BR}(D^+ \to K_S K^+) = (5.2 \pm 0.6) \times 10^{-3}$. We also determine an upper limit on the branching ratio of the doubly Cabibbo-suppressed decay mode $\mathrm{BR}(D^+ \to K^+\pi^0) < 4.2 \times 10^{-4}$.

VITA

February 1, 1974 ..... Born - Baltimore, MD

September 1988-June 1992 .. San Gorgonio High School, San Bernardino, CA

June 1992-December 1993 ... United States Military Academy, West Point, NY

May 1996 ..... B.A. Physics, Cornell University, Ithaca, NY

April 2003 ..... Won back-to-back NCAA brackets to go to 2-3 vs. Klaus

FIELD OF STUDY

Studies in Experimental Particle Physics: Professor Klaus Honscheid

TABLE OF CONTENTS

Page

Abstract ii

Vita iii

List of Tables vii

List of Figures ix

Preface xii

Chapters:

1. Introduction 1

   1.1 The Standard Model 1
      1.1.1 The Forces 2
      1.1.2 The Fundamental Particles 8
   1.2 A Brief History of Charm 13

2. Theory and Motivation for Analysis 15

   2.1 Quark-diagram scheme 16
   2.2 Doubly Cabibbo-Suppressed Decays 18
   2.3 Flavor SU(3) Symmetry 19
      2.3.1 $SU(3)_F$ studies with the quark-diagram scheme 20
      2.3.2 Isospin 20

3. CESR and CLEO 23

   3.1 CESR 23
   3.2 CLEO II and II.V 26

3.2.1 Vertex Detectors 28
3.2.2 Drift Chamber (DR) 30
3.2.3 Time of Flight System (TOF) 31
3.2.4 Crystal Calorimeter (CC) 32
3.2.5 Superconducting Coil 33
3.2.6 Muon Tracking Chambers 33
3.2.7 Trigger and Data Acquisition 34
3.3 The CLEO II/II.V Data Sample 35
3.4 Monte Carlo (MC) 37

4. Event Selection 38

4.1 Sizes of the Decay Rates 38
4.2 Measurement of the Branching Ratio (BR) 40
4.3 D^* tagging 40
4.4 Charged Track Selection 41
4.5 π^0 Selection 43
4.6 K^0 Selection 43
4.7 Multiple Entry Rejection 44
4.8 Cuts on Observables 44
4.8.1 D^+ mass 45
4.8.2 $x_{p_{D^*}}$ 46
4.8.3 $cos\theta_{helicity}$ 47
4.8.4 Final Cuts 48

5. Maximum Likelihood Method (MLM) 49

5.1 Description of PDF Shapes 50

6. Results and Discussion 59

6.1 Efficiency 59
6.2 Systematic Errors 61
6.2.1 Systematic Error on PDF shapes 64
6.3 Final Results 66

7. Obtaining Upper Limit for $D^+ \to K^+\pi^0$ 73

8. Results of $SU(3)_F$ Breaking and Isospin Calculations 76

8.1 $SU(3)_F$ Symmetry Breaking 77
8.1.1 Isospin 79

8.2 Summary 81

Appendices:

A. Glossary of Terms 82

B. Isospin Formalism 84

C. Consistency Check – Cut Analysis 89

C.1 Event Selection for Cut Analysis 89
C.2 Efficiency Calculation 90
C.3 Results 90
C.3.1 Consistency Checks for $D^+ \to \pi^+\pi^0$ 91
C.3.2 Reproducing CBX 92-111 91
C.3.3 Looking at CLEO II and II.V independently 95

Bibliography 99

LIST OF TABLES

Table **Page**

1.1 The Fundamental Forces. *Note that the strength of the forces could differ depending on the physical properties of the particles as well as their relative distances. The values here are rough estimates[1]. 3

1.2 Properties of leptons[2]. Upper limits on mass given for all neutrinos. Values of charge given in units of the charge of the electron. Error on mass of e and μ accurate past 5 significant figures. 9

1.3 Properties of quarks[2]. Mass ranges given for all quarks except t. Values of charge are given in units of the charge of the electron. . . . 10

6.1 Raw Yields from CLEO II and II.V data using FELIX 60

6.2 Reconstruction Efficiencies and Offsets from MC 61

6.3 Systematic Errors from PDF shapes. The raw event yields returned from FELIX, along with the statistical errors, are given in the second column as a source of comparison for the systematic errors listed in the third column. 64

6.4 Correlations of parameters on $x_{p_{D^*}}$ background shape 65

8.1 Amplitudes from the quark-diagram scheme that contribute to the decay modes (see Figure 2.1). s_1 and c_1 refer to Cabibbo-suppressed and favored transitions, respectively. a is the external W-emission diagram, b is the internal W-emission diagram, and d is the W-annihilation diagram. The factor of $\sqrt{\frac{1}{2}}$ arises from the normalization condition on the π^0. 76

8.2 Isospin amplitudes for $K, D \to \pi\pi$ 80

C.1 Reconstruction Efficiencies from CLEO II and II.V MC 90

C.2 Yields from CLEO II and II.V data 91

C.3 Yields from 4s2 and 4s3 data sets 95

C.4 Yields from CLEO II and II.V data sets. 98

LIST OF FIGURES

Figure **Page**

1.1 Elementary electromagnetic interaction. The diagrams also be rotated so that the photon travels along the time-axis. 5

2.1 Six quark diagrams for a meson decaying into two mesons. Dashed lines represent W meson: (a) external W-emission, (b) internal W-emission, (c) W-exchange, (d) W-annihilation, (e) horizontal W-loop, and (f) vertical W-loop. 16

3.1 Schematic of the Cornell Electron Storage Ring. 24

3.2 Side view of CLEO II.V 27

3.3 Schematic of SVX 29

3.4 Specific ionization as a function of track momentum for a selection of tracks in hadronic data events. The theoretical expectations for each particle type are superimposed as smooth curves. 31

3.5 Hadronic cross section vs. center-of-mass energy. All Υ resonances are $b\bar{b}$ bound states, but only the $\Upsilon(4S)$ is massive enough to produce two B mesons. 36

4.1 Difference in D^+ mass distribution in MC with the mass difference cut (left) and without the cut (right). 42

4.2 Signal (left) and Background (right) shapes for D^+ mass. 45

4.3 Signal (left) and Background (right) shapes for x_{pD^*}. 46

4.4 Signal (left) and Background (right) shapes for $cos\theta_{helicity}$. 47

5.1 Comparison of $cos\theta_{helicity}$ for MC with a veto on $D_S \to K^+K_S$ (left) and without (right). 52

5.2 Comparison of $cos\theta_{helicity}$ for the left and right sideband regions of the generic anti-tagged MC of $D^+ \to K^+\pi^0$ 53

5.3 Comparison of $cos\theta_{helicity}$ for generic anti-tagged MC and sideband MC of $D^+ \to K^+\pi^0$ 53

5.4 PDF for Signal $D^+ \to \pi^+\pi^0$ 54

5.5 PDF for Background $D^+ \to \pi^+\pi^0$ 54

5.6 PDF for Signal $D^+ \to K^+\pi^0$ 55

5.7 PDF for Background $D^+ \to K^+\pi^0$ 55

5.8 PDFs for Signal $D^+ \to K^+K_s$ 56

5.9 PDFs for Background $D^+ \to K^+K_s$ 56

5.10 PDFs for Signal $D^+ \to \pi^+K_s$ 57

5.11 PDFs for Background $D^+ \to \pi^+K_s$ 57

5.12 PDFs for Signal $D^+ \to K^-\pi^+\pi^+$ 58

5.13 PDFs for Background $D^+ \to K^-\pi^+\pi^+$ 58

6.1 Efficiency Fit for Signal Modes 62

6.2 Efficiency Fit for Normalization Modes 62

6.3 Fit Variables for $D^+ \to \pi^+\pi^0$. The points are from CLEO II and II.V data (with error bars) and the red solid line is the fit from FELIX . . 68

6.4 Fit Variables for $D^+ \to K^+\pi^0$. The points are from CLEO II and II.V data (with error bars) and the red solid line is the fit from FELIX 69

6.5 Fit Variables for $D^+ \to K^-\pi^+\pi^+$. The points are from CLEO II and II.V data (with error bars) and the red solid line is the fit from FELIX 70

6.6 Fit Variables for $D^+ \to K^+K_s$. The points are from CLEO II and II.V data (with error bars) and the red solid line is the fit from FELIX 71

6.7 Fit Variables for $D^+ \to \pi^+K_s$. The points are from CLEO II and II.V data (with error bars) and the red solid line is the fit from FELIX 72

7.1 Distribution of $D^+ \to K^+\pi^0$ Signal Yields - 90% C.L. at 57.20 75

C.1 Data Yield for $D^+ \to \pi^+\pi^0$ using 4s2 - 4sT 92

C.2 Data Yield for $D^+ \to K^+\pi^0$ using 4s2 - 4sT 93

C.3 Data Yield for $D^+ \to K^-\pi^+\pi^+$ using 4s2 - 4sT 94

C.4 Data Yield for $D^+ \to \pi^+\pi^0$ using 4s2 4s3 96

C.5 Data Yield for $D^+ \to K^-\pi^+\pi^+$ using 4s2 and 4s3 97

PREFACE

SENATOR JOHN PASTORE: Is there anything connected with the hopes of this accelerator that in any way involves the security of this country?

ROBERT R. WILSON: No sir. I don't believe so.

PASTORE: Nothing at all?

WILSON: Nothing at all.

PASTORE: It has no value in that respect?

WILSON: It has only to do with the respect with which we regard one another, the dignity of men, our love of culture. It has to do with, are we good painters, good sculptors, great poets? I mean all the things we really venerate and honor in our country and are patriotic about. It has nothing to do directly with defending our country except to make it worth defending. – *An excerpt from hearings of the Joint Congressional Committee on Atomic Energy, 1969*

CHAPTER 1

Introduction

> One can diagram the entire standard model on a T-shirt ... However, the standard-model T-shirt cheats. With its twelve particles and four forces, it is remarkably accurate. But it is also incomplete and, in fact, internally inconsistent. To have room on the T-shirt to make succinct excuses for the inconsistencies would require an X-tra large, and we'd still run out of shirt. *–Leon Lederman, "The God Particle"*

The reductionist philosophy has been the underlying motif for most of the physical sciences - the idea that we can understand the universe by understanding its fundamental components has driven scientists from the earliest of times. The Greek philosopher Empedocles first hypothesized that everything was composed of four fundamental components, or "elements": fire, water, air, and earth. Our continual probing into the structure of matter has brought us to the current set of fundamental components: six "leptons" and six "quarks". These components, combined with the three of the four forces that govern their interactions, are detailed in what is referred to as "The Standard Model of Fundamental Particles and Interactions", or more concisely, "The Standard Model".

1.1 The Standard Model

The Standard Model has been very successful in describing almost all of the experimental observations from particle experiments to date, spanning an energy

range up to a few hundred GeV[3]. Physicists have found that certain symmetries exist, with regards to the fundamental particles, that are intimately related to the forces that govern their interactions. The Standard Model is a quantum field theory that is based on these symmetries, called "gauge symmetries (see Appendix A), elegantly describing the universe through twelve fundamental particles and the manner in which they interact.

Although it is currently the best theory describing particle physics, there are many shortcomings of the Standard Model. For instance, there are several independent parameters that it requires as input before it can make a single prediction[3]. The fact that gravity is not included within it is also a sign that there is still much to be learned about the nature of matter.

Understanding that this model is not complete, the goal of the experimental particle physicist has been to test various aspects of the Standard Model. For times when these tests cannot be explained by the theory, doors may open for physics "beyond the Standard Model". The primary motivation for my analysis is to conduct such tests which will examine predictions of the Standard Model, especially with regards to the strong force, which is understood the least among the forces. I will first begin with a description of the Standard Model.

1.1.1 The Forces

There are four known forces which govern the interactions of all matter: strong, electromagnetic, weak, and gravitational. All of these forces share two common characteristics[4]: they are all mediated by an associated particle, called a "gauge boson", and they all have a corresponding "charge" (see Table 1.1).

The gauge bosons are not considered to be constituents of matter; rather, they are mediators which have properties that determine the behavior of the corresponding force. The Standard Model states that the "matter" particles, leptons and quarks, interact by exchanging gauge bosons. This idea replaced the more classical notion of the "action-at-a-distance" forces.

Force	Strong	Electromagnetic	Weak	Gravitational
Gauge Boson	gluons (g)	photon (γ)	$W^{\pm}$, Z	graviton
Charge	color	electric	weak isospin	mass
Strength*	10	10^{-2}	10^{-13}	10^{-41}
Mass (GeV/c^2)	0	0	80.42, 91.19	0
Spin	1	1	1	2
Range (m)	$< 10^{-15}$	∞	$10^{-18} \sim \frac{\hbar}{M_W c}$	∞

Table 1.1: The Fundamental Forces. *Note that the strength of the forces could differ depending on the physical properties of the particles as well as their relative distances. The values here are rough estimates[1].

Arguably the most commonly known charge is the electric charge. Each force, however, has a charge associated with it (see Table 1.1) which is an inherent property of matter particles. Depending on the values of these charges, particles will respond a particular way when subject to the four forces. The effects of the charges are further detailed in the following description of the four forces.

Gravitation

The gravitational force is actually not included in the Standard Model. This may initially seem surprising, given that of the four forces, gravity seems to be the most evident. The reason gravity is so evident, however, is because it is cumulative

depending on an object's gravitational charge: mass. The larger the mass, the greater the gravitational force; there is no "negative" mass charge to cancel out the "positive" mass charge; this is not the case for the charges of the other three forces. Larger objects tend to have a balanced number of positively and negatively charged particles, so the electromagnetic forces cancel, and strong and weak interactions are only valid for small ranges.

The situation is different at the subatomic scale. When dealing with subatomic particles, as seen from Table 1.1, the strength of the gravitational force is exceedingly less than those of the other forces. To date, the graviton (the gauge boson for gravity) has not been observed and the measured effects of gravity are negligible at the subatomic scales compared to the other three forces. In addition, attempts to apply gravity to a quantum mechanical system have been unsuccessful[4]. However, we have included this brief discussion of gravity for completeness.

Electromagnetic Force

Of the four forces, electromagnetism is the most thoroughly understood. The electrical charge is the most familiar and often is used as the default assumption when referring to "charge". Particles which interact electromagnetically possess either a positive or negative electrical charge. The dynamics are so well-described that it is the base-model for the dynamical theories of the other forces[1].

The gauge boson for electromagnetism is the photon; it is both massless and electrically neutral. All electromagnetic interactions can be reduced to the exchange of photons between electrically charged particles, which is the basis for Quantum Electrodynamics (QED)[1].

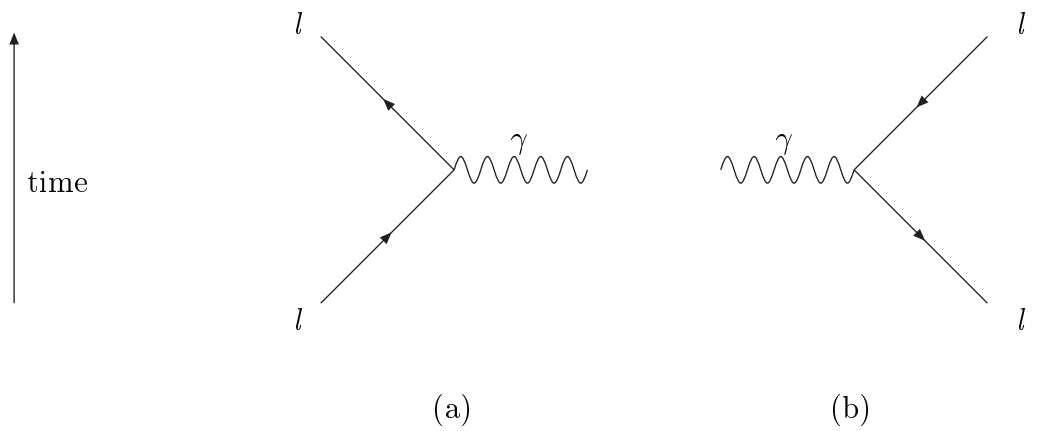

Figure 1.1: Elementary electromagnetic interaction. The diagrams also be rotated so that the photon travels along the time-axis.

Figure 1.1 is an example of a "Feynman diagram"; this figure explains the basic QED process. The solid lines represent the particles interacting electromagnetically, and the wavy lines represent the gauge bosons. Electromagnetic interactions are depicted by intersections of particles with gauge bosons; each intersection is referred to as a "vertex". A vertex is associated with a "coupling constant", which describes the strength of the interaction. A word of caution: these diagrams are symbolic and used only as a means of short-hand for larger equations; they do not represent the actual physical trajectories of the particles.

Strong Force

The strong force involves the interaction of fundamental particles known as "quarks" (see Sec. 1.1.2). The most common association made with the strong force is that it is responsible for holding a nucleus together. Its relative strength

is significantly greater than the other three (see Table 1.1). Also, unlike the other forces, the strength of the strong force increases as the relative distance of the strongly-interacting particles increases, which means that we can never isolate a single strongly-interacting particle (the particle is "confined"); this results in the use of non-perturbative methods (See Appendix A) of calculation, which are more difficult than the perturbative methods used for electromagnetic and weak forces. On the other hand, this relation between distance and the strength of the strong force also means that as the particles get extremely close, the strength of the strong force decreases (known as "asymptotic freedom"). These ideas will be further discussed when talking about "quarks", which are the only particles which interact strongly.

The charge associated with the strong force is "color", which can be either "red", "green", or "blue" (this has nothing to do with color in the visual sense). Each color has a "positive" charge (R, G, B) and a "negative" charge ($\bar{R}, \bar{G}, \bar{B}$). All strong interactions and bound states of particles must be *colorless*; such states are obtained when a positive and a negative color charge ($R\bar{R}, G\bar{G}, B\bar{B}$) are combined, or when all three charges are combined together (RGB, $\bar{R}\bar{G}\bar{B}$). This colorless criterion may also be related to the aforementioned quark confinement in that it is the *color* which is confined[5], so it is not possible to observe a colored particle in a free state.

The "gluon" is the gauge boson for strong interactions. Similarly to the photon, it is massless; however it does carry the strong charge. In fact, it has two color charges associated with it, which cancel out the color charges of strongly-interacting particles in order to make the overall reaction colorless. The fact that gluons carry color also means that they can interact with other gluons (the force is "non-Abelian").

Weak Force

The weak force was originally introduced when attempting to explain nuclear radioactivity. It was Enrico Fermi in 1933 who explained that a neutron could decay into a proton, and electron, and an (anti-)neutrino via this interaction[6].

Today, we have fairly good understanding of this interaction. It is unique because unlike the other three forces, *all* matter particles can interact weakly. Matter particles can be broken down into a "left-handed" component and a "right-handed" component (except for those which are massless, which have only a left-handed component); the handedness of a particle refers to the relation of the spin state of the particle and its direction of motion (see Appendix A under **helicity**). All of the matter particles are grouped into left-handed pairs, or "doublets"; the elements in each doublet have either a positive or negative weak charge, or "weak isospin". Such pairings do not exist for the right-handed components, hence forming "singlets"; these singlets do not interact weakly. The weak transition is the only one which may result in a change of the flavor of a particle. The weak doublets and transitions are further discussed in Sec. 1.1.2.

The gauge bosons for the weak interactions are the $W^{\pm}$ and the Z^0. These gauge bosons differ from those of the other forces in that they are massive (see Table 1.1). The existence of massive gauge bosons actually explains the short range of the weak force as well as its relative (lack of) strength compared to the electromagnetic force[1]. Also note that the charges denoted on the $W^{\pm}$ and Z^0 refer to their electrical charge, and not their weak charge.

1.1.2 The Fundamental Particles

As mentioned before, the fundamental components of all matter consist of six types (or "flavors") of leptons and six flavors of quarks. Each particle also has a corresponding "antiparticle", which has exactly the same mass as its counterpart, but oppositely-signed additive quantum numbers (such as electric charge). We consider these particles to be fundamental because there seems to be no substructure up to our present experimental limits determined by the LEP experiments.

The leptons and quarks are classified as "fermions", which means that they possess a half-integer value for "spin" (see Appendix A). These particles can also be grouped into three "families", each containing two leptons and two quarks (see Tables 1.2,1.3). If we were to ignore the mass differences between the particles, the three families would be indistinguishable[3].

Leptons

There are three charged leptons; the most common and well-known of these is the electron (e). The other two are the muon (μ) and the tau (τ) which have the same properties of the electron, but are significantly heavier (see Table 1.2). Each charged lepton has a corresponding neutral lepton, known as a neutrino (ν_l), where the subscript, l, refers to the flavor of charged lepton. Table 1.2 shows the current upper limits on the mass of each flavor of neutrino. Neutrinos were originally thought to be massless, but recent studies of neutrino oscillations[7] have given evidence that they are massive, albeit very small. The limits listed in Table 1.2 do not take oscillations into consideration.

Family	Flavor	Mass (MeV/c^2)	Electric Charge	Weak Charge
I	ν_e	$< 3 \times 10^{-6}$	0	$+1/2$
	e	0.51	-1	$-1/2$
II	ν_μ	< 0.19	0	$+1/2$
	μ	105.66	-1	$-1/2$
III	ν_τ	< 18.2	0	$+1/2$
	τ	$1776.99^{+0.29}_{-0.26}$	-1	$-1/2$

Table 1.2: Properties of leptons[2]. Upper limits on mass given for all neutrinos. Values of charge given in units of the charge of the electron. Error on mass of e and μ accurate past 5 significant figures.

The lepton families consist of an electrically-charged lepton (positive weak-charged) and its corresponding neutrino (electrically-neutral, negatively weak-charged). As mentioned previously, weak interactions change the weak charge of a particle. While electrically-neutral weak interactions (Z^0) maintain the flavor of the lepton, electrically-charged weak interactions ($W^\pm$) result in a flavor change of the lepton (for example, an electron converts into an electron-neutrino). Transitions between families (electron to a muon-neutrino), however, are not allowed for the leptons[1].

Quarks

In 1968, physicists at the Stanford Linear Accelerator Center (SLAC) discovered that the proton and neutron (previously believed to be fundamental particles) were composed of smaller particles: "quarks". The etymology of quarks comes from James Joyce's *Finnegan's Wake*. Murray Gell-Mann, who had predicted the existence of quarks a few years prior, had been influenced by the line "three quarks for

[1]With the discovery of neutrino oscillations, transitions between families may possibly occur.

Muster Mark." Given that, at the time, they only predicted the existence of three quarks (u, d, s), this seemed all the more appropriate[6].

We know today that there are six quarks (see Table 1.3). Quarks have positive color charges, and anti-quarks have negative color charges (Sec 1.1.1). To remain colorless, bound states of quarks consist of two types of combinations: a quark and an anti-quark, also known as a "meson", or three quarks each having a different color, also known as a "baryon". Almost all the matter in the universe is composed of two baryons: protons (uud) and neutrons (udd). Using particle accelerators, however, we are able to create other mesons and baryons, albeit extremely short-lived.

Family	Flavor	Mass (GeV/c^2)	Electric Charge	Weak Charge
I	up	$0.0015 - 0.0045$	$+2/3$	$+1/2$
	$d$own	$0.005 - 0.0085$	$-1/3$	$-1/2$
II	$c$harm	$1.0 - 1.4$	$+2/3$	$+1/2$
	$s$trange	$0.080 - 0.155$	$-1/3$	$-1/2$
III	$t$op	174.3 ± 5.1	$+2/3$	$+1/2$
	$b$ottom	$4.0 - 4.5$	$-1/3$	$-1/2$

Table 1.3: Properties of quarks[2]. Mass ranges given for all quarks except t. Values of charge are given in units of the charge of the electron.

Similarly to the leptons, the quark families consist of one positively and one negatively weak-charged quark. However, unlike the leptons, weak interactions are not restricted to quarks within a family. For quarks, the weak interactions couple positively weak-charged quarks with a linear combination of all three negatively weak-charged quarks. The development of this idea began in 1963 with a paper by Nicola Cabibbo[8], when only the u, d, and s quarks were known. He suggested

that there is a factor of $cos\theta_c$ in the vertex (see Sec. 1.1.1) of $d \rightarrow u$ transitions and a factor of $sin\theta_c$ in $s \rightarrow u$ transitions, where θ_c referred to the "Cabibbo angle". The value of $sin\theta_c$ was experimentally found to be 0.22 degrees, which means that the process of $s \rightarrow u$ is "Cabibbo-suppressed" compared to the "Cabibbo-favored" $d \rightarrow u$ transition.

With the Cabibbo theory and with analogy to the doublets formed by the leptons, it was postulated that a doublet could be formed with the electrically-charged $+\frac{2}{3}$ quark with a rotated superposition of the two electrically-charged $-\frac{1}{3}$ quarks:

$$\begin{pmatrix} u \\ d\ cos\theta_c + s\ sin\theta_c \end{pmatrix}$$

where θ_c was the Cabibbo angle and this rotated superposition of flavor eigenstates was the "mass" or weak eigenstate; meaning that weak interactions would couple a u to $d\ cos\theta_c + s\ sin\theta_c$ rather than to d and s individually. There arose a problem with this though in that with only one doublet, flavor-changing neutral current transitions should be possible; that is, $s \rightarrow d$ and $d \rightarrow s$ transitions are allowed in this model[9]. At the time, however, no experimental evidence of these transitions existed.

In 1970, Glashow, Iliopoulos, and Maiani (GIM) hypothesized the existence of a fourth quark[10]; this later turned out to be the "charm" quark. There were now two doublets and two mass eigenstates, d' and s'. The relation between mass and flavor eigenstates became

$$\begin{pmatrix} d' \\ s' \end{pmatrix} = \begin{pmatrix} cos\theta_c & sin\theta_c \\ -sin\theta_c & cos\theta_c \end{pmatrix} \begin{pmatrix} d \\ s \end{pmatrix} \tag{1.1}$$

where θ_c was the Cabibbo angle and the 2×2 matrix is known as the "mixing" matrix. Having the $-sin\theta_c$ term in the mixing matrix resulted in the cancellation of the $s \to d$ and $d \to s$ transitions.

In 1973, Kobayashi and Maskawa[11] extended this model to six quarks, producing a unitary 3×3 matrix; this relation is known today as the "Cabibbo-Kobayashi-Maskawa" (CKM) matrix. The quark families are now rewritten as

$$\begin{pmatrix} u \\ d' \end{pmatrix}_L \begin{pmatrix} c \\ s' \end{pmatrix}_L \begin{pmatrix} t \\ b' \end{pmatrix}_L \tag{1.2}$$

where d', s', and b' are the mass eigenstates. The relation between the mass and flavor eigenstates for these three quarks is written as

$$\begin{pmatrix} d' \\ s' \\ b' \end{pmatrix}_L = \begin{pmatrix} V_{ud} & V_{us} & V_{ub} \\ V_{cd} & V_{cs} & V_{cb} \\ V_{td} & V_{ts} & V_{tb} \end{pmatrix} \begin{pmatrix} d \\ s \\ b \end{pmatrix}_L \tag{1.3}$$

where the 90% confidence limits on the magnitude of the elements of the matrix are[2]

$$\begin{pmatrix} 0.9741 - 0.9756 & 0.219 - 0.226 & 0.0025 - 0.0048 \\ 0.219 - 0.226 & 0.9732 - 0.9748 & 0.038 - 0.044 \\ 0.004 - 0.014 & 0.037 - 0.044 & 0.9990 - 0.9993 \end{pmatrix}. \tag{1.4}$$

This shows that transitions within families (along the diagonal) occur most often, while transitions across families (off-diagonal elements) are suppressed.

A unitary $N \times N$ matrix will have $\frac{N(N-1)}{2}$ real parameters and $\frac{(N-1)(N-2)}{2}$ imaginary parameters[9]. For the CKM matrix, this gives 3 real and 1 imaginary parameters. While there are several parameterizations of the CKM matrix, the standard parameterization[2] is given by

$$\begin{pmatrix} d' \\ s' \\ b' \end{pmatrix}_L = \begin{pmatrix} c_{12}c_{13} & s_{12}c_{13} & s_{13}e^{-i\delta_{13}} \\ -s_{12}c_{23} - c_{12}s_{23}s_{13}e^{i\delta_{13}} & c_{12}c_{23} - s_{12}s_{23}s_{13}e^{i\delta_{13}} & s_{23}c_{13} \\ s_{12}s_{23} - c_{12}c_{23}s_{13}e^{i\delta_{13}} & -c_{12}s_{23} - s_{12}c_{23}s_{13}e^{i\delta_{13}} & c_{23}c_{13} \end{pmatrix} \begin{pmatrix} d \\ s \\ b \end{pmatrix}_L. \tag{1.5}$$

where $c_{ij} = cos\theta_{ij}$ and $s_{ij} = sin\theta_{ij}$, with the subscripts $i, j = 1, 2, 3$ referring to the families I, II, and III. The complex phase, δ_{13}, introduces a term in the matrix that allows the decay rates of particles and corresponding anti-particles to differ if it has a non-zero value, leading to CP violation (see Appendix A). In the limit of $\theta_{13} = \theta_{23} = 0$, the matrix reduces to the Cabibbo mixing where $\theta_{12} = \theta_c$. Cabibbo-favored decays involve transitions along the diagonal elements of the CKM matrix, and Cabibbo-suppressed refer to transitions involving the off-diagonal elements.

1.2 A Brief History of Charm

This analysis deals with the decay of mesons involving charm quarks: "charm physics". Charm physics allows us to study constants of nature, such as the CKM matrix elements V_{cd}, V_{cs}, and V_{cb}. It also provides a laboratory for studies of the strong interactions, which are hard to calculate within the framework of the Standard Model because of its non-perturbative nature (see Sec. 1.1.1). I offer here a short history regarding the development of charm physics.

In 1964, Sheldon Glashow and James Bjorken hypothesized the existence of the charm quark[12]. At that time, there were only three known quarks: up, down, and strange. Influenced by the two doublet structure for the four known leptons at the time (e, ν_e, μ, μ_e), they noted that among other things, a fourth quark would return symmetry between the leptons and quarks. The development of the GIM mechanism (see Sec. 1.1.2) to explain the absence of flavor-changing neutral currents as well as the suppression of the $K^0 \to \mu^+\mu^-$ decay further supported the existence of charm.

In 1968, Leon Lederman's dimuon experiment showed signs of the existence of this fourth quark, but unfortunately this discovery went unpublished[6]. The world

would have to wait for the "November Revolution" of 1974 to confirm the existence of the charm quark. On November 11, 1974, groups at SLAC and Brookhaven both produced clear evidence for a resonance at 3.105 GeV. This resonance, called the J/ψ, turned out to be a bound state of a charm quark and its anti-quark ($\bar{c}$). The discovery of the D^0 ($c\bar{d}$) at SLAC followed shortly after in 1976 and the rest is history.

The excitement over charm mesons has diminished somewhat with the discovery of the bottom and top quarks. Charm mesons, however, continue to be studied because of their unique position. They are light enough not to be considered a heavy quark, and heavy enough not to be considered a light quark. Their mass puts them squarely in the midst of many resonances sharing close to the same mass. Searches for CP-violation and mixing in charm, both of which are predicted to be extremely small, can open doors for possibilities for new physics. What follows is a description of my measurement of three decay rates and its humble impact on testing the Standard Model.

CHAPTER 2

Theory and Motivation for Analysis

> Science is built up with facts, as a house is with stones. But a collection of facts is no more a science than a heap of stones is a house. *–Poincaré on the need for theory*

The focus of this analysis is to use the CLEO II and II.V datasets to search for three decay modes: $D^+ \to \pi^+\pi^0$, $D^+ \to \bar{K}^0 K^+$, and $D^+ \to K^+\pi^0$, where the D^+ meson is a $c\bar{d}$ bound state, the π^+ is a $u\bar{d}$ bound state, the K^+ is a $u\bar{s}$ bound state, the π^0 is a linear combination of $u\bar{u}$ and $d\bar{d}$ states, and $\bar{K}^0$ is a $d\bar{s}$ bound state. The first two modes are singly Cabibbo-suppressed (SCS) while the latter is doubly Cabibbo-suppressed (DCS) (see Sec. 1.1.2). The first two modes proved to be important for "flavor $SU(3)$ symmetry" ($SU(3)_F$) calculations (see Sec. 2.3); the final mode is interesting because, among other things, doubly Cabibbo-suppressed modes are very rare. This chapter discusses the theory that motivated the measurement of these modes. We begin with the quark-diagram scheme, which uses Feynman diagrams to describe the weak decays of mesons, then continue with a discussion of DCS decays, and conclude with a discussion about $SU(3)_F$ symmetry and its relation to isospin.

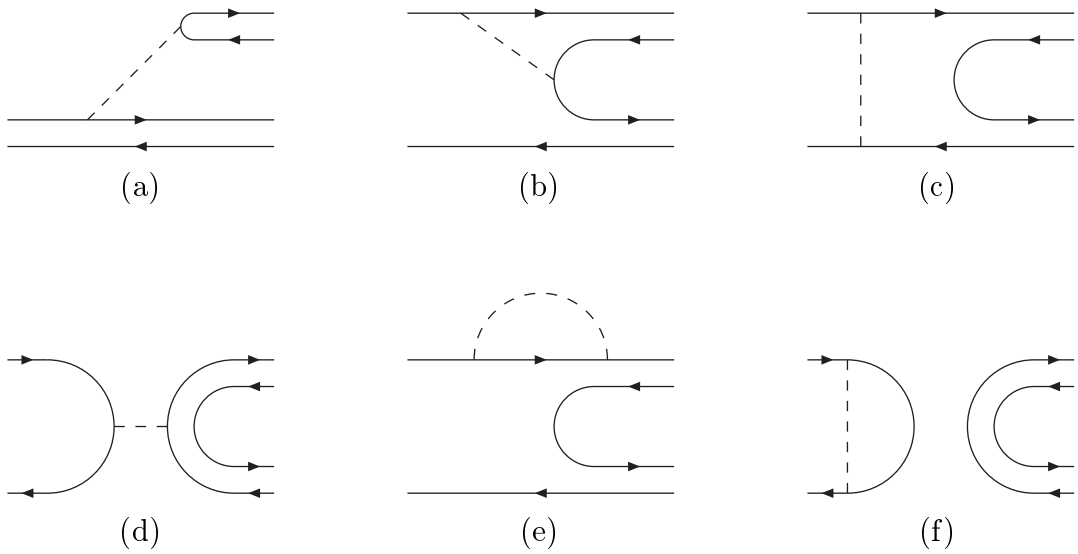

Figure 2.1: Six quark diagrams for a meson decaying into two mesons. Dashed lines represent W meson: (a) external W-emission, (b) internal W-emission, (c) W-exchange, (d) W-annihilation, (e) horizontal W-loop, and (f) vertical W-loop.

2.1 Quark-diagram scheme

To first order, all weak decays of mesons may be described using six Feynman diagrams, sometimes referred to as "quark diagrams"[13]. Figure 2.1 shows these six diagrams: (a) external W-emission, (b) internal W-emission, (c) W-exchange, (d) W-annihilation, (e) horizontal W-loop, and (f) vertical W-loop. The decays measured in this analysis can be described using three of these six diagrams: the external and internal W-emission and the W-annihilation diagrams. The contributing diagrams for each decay mode are listed below:

- $D^+ \to \pi^+\pi^0$: external and internal W-emission

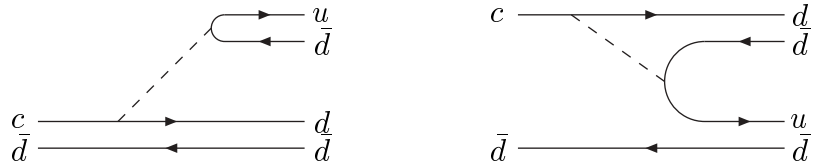

- $D^+ \to \bar{K}^0\pi^+$: external and internal W-emission

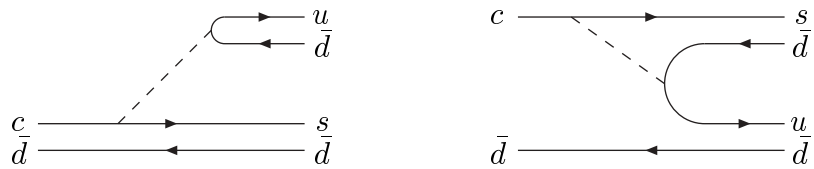

- $D^+ \to K^+\pi^0$: external W-emission and W-annihilation

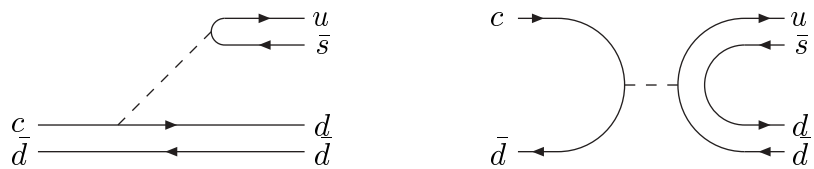

- $D^+ \to \bar{K}^0K^+$: external W-emission and W-annihilation

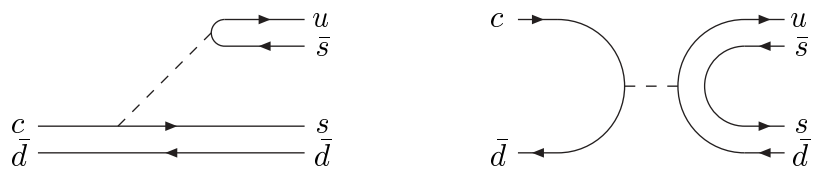

The quark diagrams represent a decay *amplitude* A_i (see Appendix A), which is related to the decay rate Γ of the initial particle to the final products via the specified process, indexed by i. Combining all contributing diagrams gives us the total decay amplitude A, which is related to the decay rate of the initial particle to the final products via all possible processes.

$$A(D^+ \to \pi^+\pi^0) = A_a(D^+ \to \pi^+\pi^0) + A_b(D^+ \to \pi^+\pi^0) \tag{2.1}$$

$$\Gamma(D^+ \to \pi^+\pi^0) \sim |A(D^+ \to \pi^+\pi^0)|^2 \tag{2.2}$$

$$\sim |A_a(D^+ \to \pi^+\pi^0) + A_b(D^+ \to \pi^+\pi^0)|^2 \tag{2.3}$$

where A_a and A_b are the decay amplitudes for the external and internal W-emission diagram, respectively.

2.2 Doubly Cabibbo-Suppressed Decays

Doubly Cabibbo-suppressed decays (DCSD) refer to decay modes that have two Cabibbo-suppressed quark transitions (Sec. 1.1.2). In the case of charm decays, this involves a $c \to d$ and $s \to u$ transition. Such decays are rare, as seen by the fact that there are currently only three measured DCSD modes in the PDG[2].

If the spectator model were very accurate, then our search for $D^+ \to K^+\pi^0$ would be invaluable to D-mixing measurements, since such measurements use interference terms from the Cabibbo-favored decay (CFD) $D^0 \to \bar{D}^0 \to K^-\pi^+$ and the DCSD $D^0 \to K^+\pi^-$, which differs only from the charged mode in the spectator $\bar{u}$ instead of $\bar{d}$. Since the D^+ decay does not include mixing, we would be able to isolate the contribution from DCSD and apply it to the neutral D-mixing study. Unfortunately, there are a lot of resonances that have a similar mass to that of the D meson; because of this, the decay of a D is highly influenced by final state interactions (FSI), which means that the D can decay, via strong force, to any number of these resonance states before decaying weakly. This means that the predictions of the spectator model can be highly skewed. Nevertheless, increased understanding of DCSD modes can significantly improve D-mixing measurements.

DCSD modes are also useful for SU(3) symmetry studies. With an increased understanding of the SCSD modes, it is a natural extension to begin testing with the DCSD modes. There are studies for DCSD modes that parallel those discussed in Sec. 2.3.

2.3 Flavor SU(3) Symmetry

A symmetry is when changes in the variables of a system do not change the essential physics. For example, if an experiment is symmetric with respect to time, then the results that it produces today will be the same as tomorrow, or in a year from now. The significance of symmetries in physics became clear in 1917, when Emmy Noether published her theorem stating that every symmetry corresponds to a conservation law[1]. For our example of the symmetry with respect to time, Noether's theorem equates this to a conservation of energy for the experiment. Studying symmetries of the fundamental particles, therefore, gives us a better understanding of the underlying physical laws which govern their actions. For my analysis, I applied my results to measure predictions of "flavor $SU(3)$" symmetry.

Historically, the advent of $SU(3)_F$ brought about the introduction of quarks into particle physics[14]. Flavor SU(3) symmetry, or $SU(3)_F$ treats the up, down, and strange (u,d,s) quarks as identical particles. We know from experiment, however, that the mass of the strange quark is significantly larger than the mass of the up or down quarks, which results in a "breaking" of this symmetry. If the level of breaking is small and well understood, then it is possible to extract useful physical predictions using this *approximate* symmetry. Current predictions using $SU(3)_F$ are accurate to around 30%[3].

Studying the size of the $SU(3)_F$ symmetry breaking has become of interest in neutral D mixing studies. It has been shown that the mass and width differences (x, y) in the CP-eigenstates of the neutral D mesons are dependent on $SU(3)_F$ symmetry breaking[15]. In the hopes that x and y are experimentally found to be non-zero, a very good theoretical prediction of x and y within the Standard Model is

necessary to introduce the possibility for "new physics". This is only possible if the size of $SU(3)_F$ breaking is well-determined. Our analysis uses decays from charged D mesons to measure ratios that are significant for $SU(3)_F$ symmetry breaking studies.

2.3.1 $SU(3)_F$ studies with the quark-diagram scheme

Using the quark-diagram scheme, $SU(3)_F$ symmetry studies may be conducted by observing decays which have the same quark diagrams contributing to the total decay amplitude, but differing in the existence of an s instead of a d. For example, both the decay $D^+ \to \pi^+\pi^0$ and $D^+ \to K_S\pi^+$ have only the external W-emission and the internal W-emission diagrams contributing to the final decay amplitude. The difference is that the former has a $c \to d$ transition and the latter has a $c \to s$ transition. Comparisons of the decay rates of these two modes will therefore give us information about $SU(3)_F$.

Also essential is understanding the dynamical assumptions regarding the quark diagrams when applying this scheme, such as the relative size of the diagrams or interference between different diagrams[16]. The $D^+ \to K_S K^+$ mode has a contribution from an external W-emission diagram and a W-annihilation diagram. Comparison of this mode with the above-mentioned modes can give insight into the interference terms between the external and internal W-emission diagrams as well as the relative size of the W-annihilation term.

2.3.2 Isospin

Before it was known that the proton and neutron had substructure, Heisenberg suggested that they could actually be two different states of the same particle: a

nucleon[1]. The only major difference between them seemed to be that the proton had a positive electric charge, and the neutron was electrically neutral; the neutron was also heavier than the proton, but very marginally. Heisenberg's claim was that if we looked only at the strong force, there existed a symmetry with these particles; given that this situation paralleled that of the electron having two spin states, this new symmetry was called *isospin*.

We know today that the differences in the substructure of a proton and neutron can be traced to the difference between a u and d quark (Sec. 1.1.2). Isospin symmetry therefore involves the interchangeability of these two quarks, and can be classified as an SU(2) group. This is generally considered to be a more reliable symmetry than $SU(3)_F$[16] because the mass difference between the u and d quarks are much closer than the mass difference between the s and u, d quarks; we can rewrite the decays of particles from their quark-flavor representation to an isospin representation. For this analysis, I present the ratio of isospin amplitudes using my measurement of the decay rate of $D^+ \to \pi^+\pi^0$ and the PDG[2] values for the decay rates of $D^0 \to \pi^+\pi^-$ and $D^0 \to \pi^0\pi^0$. The phase between the isospin amplitudes also gives information regarding FSI. For comparison, the isospin amplitudes for the $K \to \pi\pi$ system are also given.

$\Delta I = \frac{1}{2}$ Rule

The well known problem of the "$\Delta I = \frac{1}{2}$ Rule" states that a particle will decay to a final state where $\Delta I = |I_{final} - I_{initial}| = \frac{1}{2}$. If we look at a two π system, Bose statistics tells us that their total isospin can only be 0 or 2. Therefore, if this rule

[2]The PDG refers to the 2002 Edition of the "Review of Particle Physics" released by the Particle Data Group

were exact, a meson having $I = \frac{1}{2}$ (such as a K or D) decaying into two πs would necessarily have $I = 0$ as the final state.

This rule has been well documented for $K \to \pi\pi$ decays[17]. The amplitude for the $\Delta I = \frac{1}{2}$ decay is approximately 22 times larger than that for the $\Delta I = \frac{3}{2}$ decay[3], giving strong support for the $\Delta I = \frac{1}{2}$ rule. Unfortunately, there still is not a good theoretical explanation for this phenomenon. Studies involving other mesons may therefore be useful in interpreting this result. For this analysis, I use our measurements to calculate the isospin amplitudes for $D \to \pi\pi$.

CHAPTER 3

CESR and CLEO

For those of us doing Charm Physics, the Resonance itself is an annoying Background! *–Don Fujino*

3.1 CESR

The Cornell Electron-positron Storage Ring (Fig. 3.1) is an e^+e^- collider, 768 meters in circumference, which is capable of producing center-of-mass energies between 9 - 12 GeV.

The process of producing these collisions begins with the emission of electrons from a heated filament, which are then accelerated through a 30 meter linear accelerator (LINAC) to approximately 300 MeV. At this point, the LINAC passes the electrons into the synchrotron. To create positrons, the electrons from the filament are directed toward a tungsten plate midway through the LINAC. The collisions between the electrons and the plate produce e^+e^- pairs and X-rays. Using magnets, the positrons are separated from the electrons and the X-rays, accelerated to 200 MeV through the remaining part of the LINAC, and then injected into the synchrotron.

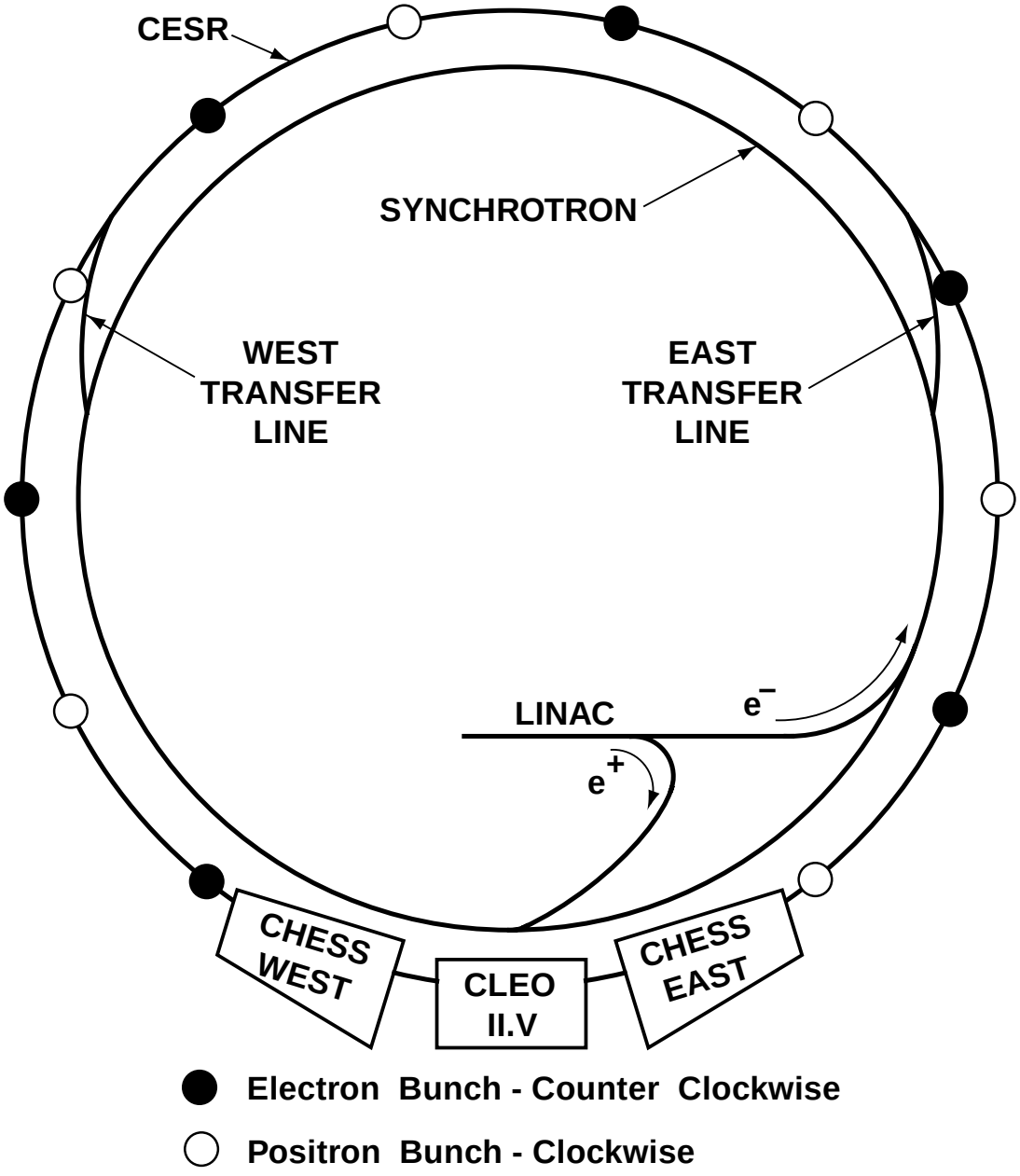

Figure 3.1: Schematic of the Cornell Electron Storage Ring.

Once inside the synchrotron, the particles are guided in a circular orbit using bending magnets. They make 4,000 laps around the ring (in about $\frac{1}{100}$ s), accelerating to an energy of 5.29 GeV. When the particles reach this energy, they are passed into a storage ring; the positrons go through this first in a clockwise direction, and then the electrons, in a counter-clockwise direction.

Whereas each particle spends a fraction of a second in the synchrotron, they must spend a half-hour to an hour rotating around the storage ring. While in the ring, particles radiate a half-megawatt of *synchrotron radiation*, causing the particle to lose energy and the inner wall to heat. This heat is carried away by water and the energy lost by the particle from this radiation is restored in the beam by radio-frequency (RF) cavities.

The number of interactions a collider produces is parameterized by its luminosity, which is defined as the rate of interactions per unit of cross-section for a given process. Physically, this tells us that the number of interactions produced in the accelerator at a given instant of time is the product of the instantaneous luminosity and the cross-section (σ) of the decay of interest (Eq. 3.1)

$$N = \mathcal{L}\sigma. \tag{3.1}$$

To determine the total number of events produced in a given amount of time, such as the life of a detector, we substitute the *integrated* luminosity ($L = \int \mathcal{L} dt$) into Eq. 3.1.

The particle beams are not continuous, but rather, divided into *bunches*. Also, the collisions are at a small crossing-angle rather than head on. These two properties of the beams enable the collider to reach higher currents of particles, which result in a larger luminosity. The generalized formula for the instantaneous luminosity[18]

is given by Eq 3.2

$$\mathcal{L} = \frac{fB\mathcal{N}_1\mathcal{N}_2}{4A_{eff}} \tag{3.2}$$

where f is the frequency that the bunches circulate around the storage ring, B is the number of bunches, $\mathcal{N}_1$ and $\mathcal{N}_2$ are the number of particles *per bunch*, and A_{eff} is the effective projected area of interaction for the two beams. Peak instantaneous luminosity for CESR is roughly $8 \times 10^{32} cm^{-2} s^{-1}$ and the cross section for $e^+e^- \to c\bar{c}$ is 1.3 nb, or $1.3 \times 10^{-33} cm^2$; this gives a peak rate of about 1 event per second.

3.2 CLEO II and II.V

This analysis used data from the CLEO II and CLEO II.V detectors. The detector elements, beginning from the Beryllium beam pipe (3.5 cm in radius for CLEO II and 2.0 cm for CLEO II.V) and working radially outward, are the vertex detectors, the central detector drift chambers (DR), the time of flight system (TOF), the crystal calorimeter (CC), a superconducting coil and the muon tracking system (MU). A full description of the CLEO II detector is given in Ref. [19]. A brief discussion of the detector components follows in the sections of this chapter.

There were two major differences between these two detectors. First, the gas used in the drift chamber was changed from Argon-Ethane to Helium-Propane, improving the cell efficiency for the drift chamber. The second change was to the inner vertex detector and discussed in Sec. 3.2.1.

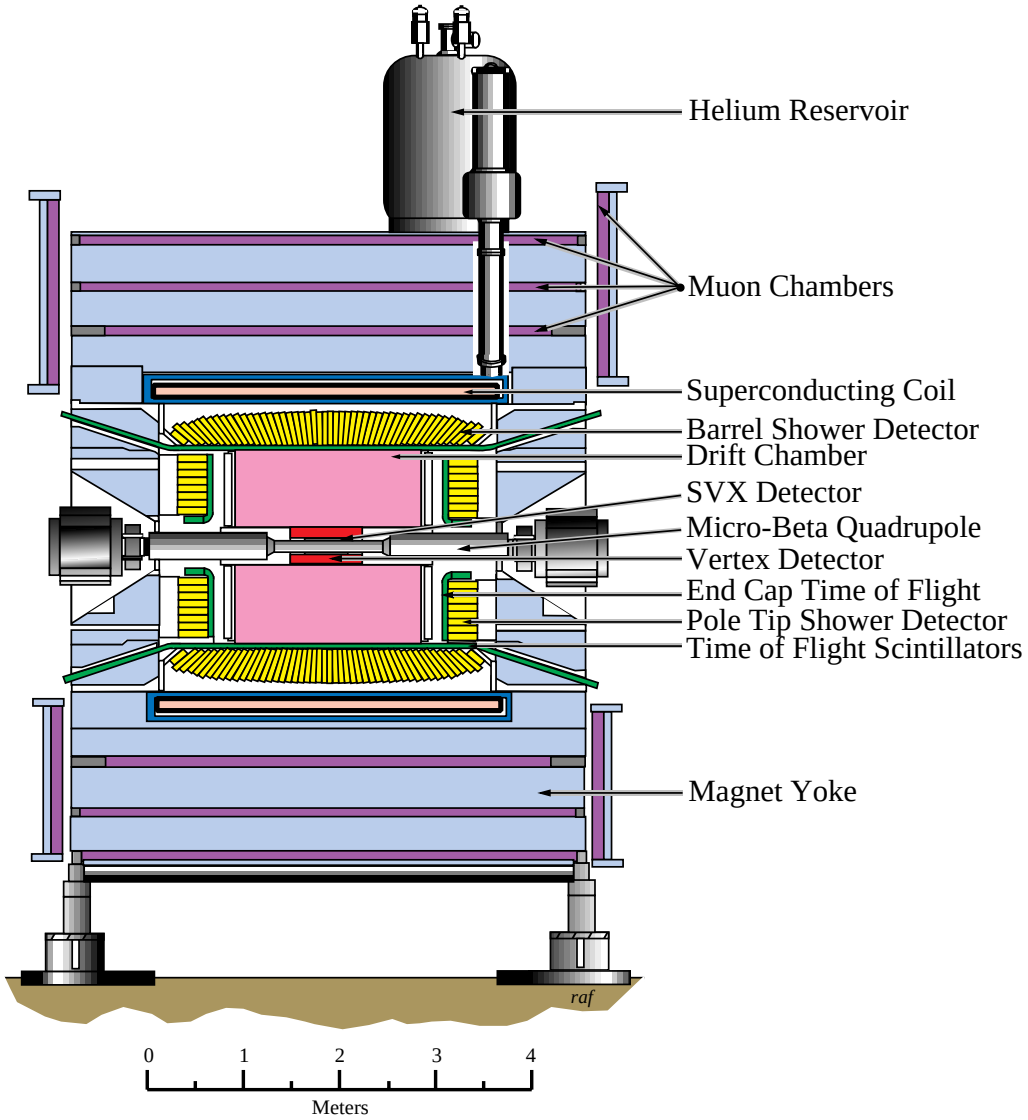

Figure 3.2: Side view of CLEO II.V

3.2.1 Vertex Detectors

Vertex detectors are used for precision measurements on track trajectory for charged particles and to reconstruct the interaction point. The CLEO vertex detector consisted of an outer and an inner vertex detector. The outer vertex detector (VD), remained the same for both CLEO II and II.V. The inner vertex detector, however, went through a modification. For CLEO II (prior to April 1995), the inner vertex detector consisted of Precision Tracking Layers (PTL). In CLEO II.V, this was replaced with a Silicon Vertex Detector (SVX) for improved precision tracking.

Precision Tracking Layers (PTL)

The purpose of the PTL was to measure the transverse particle direction near the interaction point. It consisted of a six-layer straw tube drift chamber, extending from 3.5 cm to 7.5 cm, in the CLEO II detector. Each layer consisted of 64 axial gold-plated tungsten wires held at a positive high voltage and each wire was surrounded by an aluminized Mylar tube held at ground. The single-hit resolution of this detector was 50 μm.

Silicon Vertex Detector (SVX)

In the SVX (see Figure 3.3), particles passing through the detector create electron-hole pairs along its trajectory; these pairs are gathered on sensitive strips in the silicon. The fine pitch strips allowed the SVX to have better resolution than the PTL despite being smaller.

The active element of the SVX consisted of double-sided silicon wafers 300μm thick. The outward facing sensitive strips run along the beam line and measure $r-\phi$ trajectories with a resolution of 18 μm. The inward facing strips run perpendicular

to the beam line and measure $r - z$ trajectories with a resolution of 28 μm. The SVX has three layers: the first located right outside the beam pipe at 2.35 cm, the second at 3.25 cm, and the outermost at 4.8 cm. The 96 silicon wafers are arranged into eight octants of twelve wafers. Both sides of the silicon wafers read out into 26,208 channels for the entire SVX.

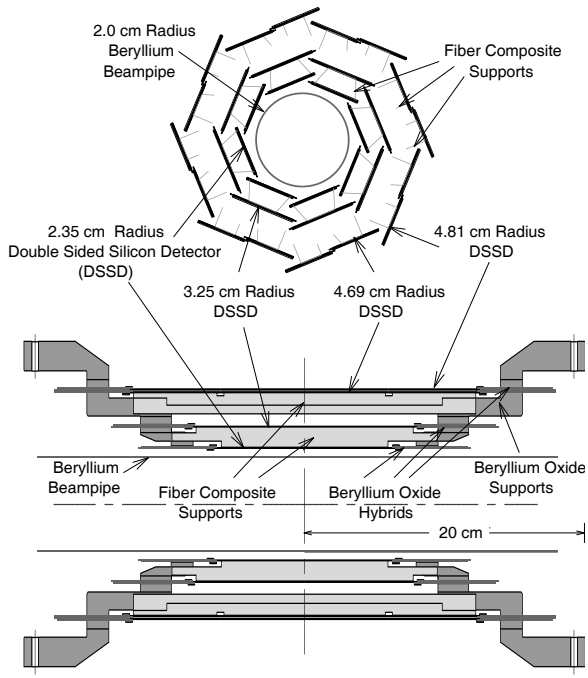

Figure 3.3: Schematic of SVX

(Outer) Vertex Detector (VD)

The VD was originally used as the primary vertex detector for CLEO in 1984. For the CLEO II and II.V detectors, it was used primarily to measure the transverse

momentum (p_T) for particles possessing low p_T. It is a 10-layer drift chamber, extending from 8.1 cm to 16.4 cm, that is composed of 800 high voltage *sense* wires and 2272 *field* wires, arranged in hexagonal cells that give radial track information. The sense wires have enough resistance to create different currents depending on the distance traveled; z information may therefore be obtained by reading out the sense wires from both ends and measuring the difference in the currents. This method is known as *charge division*. Using a gas composed of 50% argon and 50% ethane gives a single-hit resolution of 150 μm in $r - \phi$ and 750 μm in z.

3.2.2 Drift Chamber (DR)

The DR provides most of the track curvature measurement as well as the $\frac{dE}{dx}$ for charged particles, essential for particle identification. The DR extends radially from 17.5 cm to 95 cm and has a length of 2.15 m. There are a total of 12,240 high voltage, gold-plated tungsten *sense* wires and 36,240 *field* wires arranged in 51 layers of 14 mm $\times$ 14 mm square cells. Of these 51 layers, 40 are composed of axial wires for measuring momenta that are transverse ($x - y$) from the beam pipe and 11 are composed of wires with a small *stereo* angle ($3^\circ - 7^\circ$) for obtaining information in the z direction. The axial sense wires are staggered by half a cell between layers to reduce left-right ambiguities. Aluminum endplates 3.175 cm thick provide mechanical support for the wires.

The energy lost by particles traversing the DR is recorded, allowing us to obtain $\frac{dE}{dx}$ information for particle identification. From Figure 3.4, we see that different particles will deposit different amounts of energy for a given value of momentum

(although this difference significantly decreases for higher momenta). A description of how to use this information is given in Ch. 4.

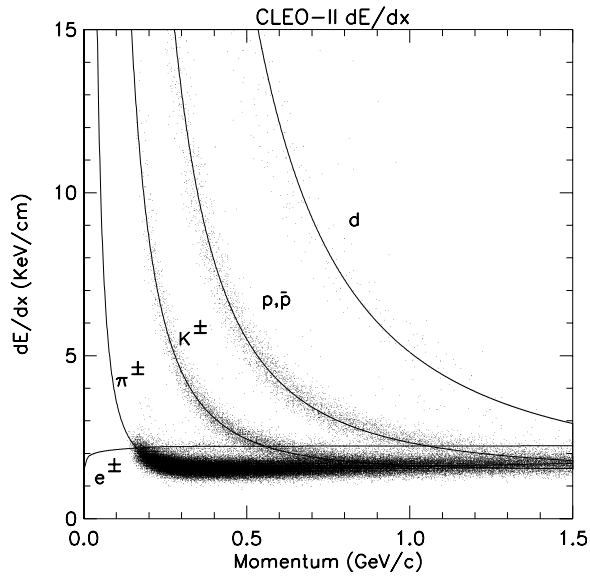

Figure 3.4: Specific ionization as a function of track momentum for a selection of tracks in hadronic data events. The theoretical expectations for each particle type are superimposed as smooth curves.

3.2.3 Time of Flight System (TOF)

The TOF system measures the time of flight of particles traveling through the detector by measuring the time interval between the e^+e^- collision and the arrival of a track passing through the detector. The TOF is used for particle identification as well as a first-level trigger for tagging interesting events. The system consisted of 64 scintillators (5 cm thick $\times$ 10 cm wide $\times$ 279 cm long) around the barrel and 28 wedge-shaped scintillators (5 cm thick) for each endcap; together, the TOF system

covers 96% of the solid angle. The timing resolution of the system is 150 ps in the barrel and 270 ps in the endcap.

3.2.4 Crystal Calorimeter (CC)

The primary purpose of the CC is to measure the energy and direction of neutral particles and electrons. As particles pass through the CC, they deposit some energy into the crystal, producing scintillation light that is then read-out by four photo-diodes at the end of each crystal. The CC was essential for my analysis, where reconstructed π^0s were used for all modes.

7800 thallium-doped Cesium Iodide (CsI) crystals (5 cm thick $\times$ 5 cm wide $\times$ 30 cm long) made up the CC and stretch from an inner radius of 1.0 m to an outer radius of 1.4 m, covering 95% of the solid angle. There are two parts to the CC: the barrel detector and two endcap detectors. The barrel detector consists of 6144 CsI crystals arranged in 48 rows along the z-direction, providing angular coverage down to 32°. The other 1656 crystals are arranged into two concentric ring-shaped aluminum holders at each end of the detector and have an angular coverage of $5^\circ - 36^\circ$.

The performance of the CC depends on the amount of material between the interaction point and the crystals. The best resolution is obtained in the the "good barrel" region, which corresponds to an angle of $36^\circ - 144^\circ$ (or $cos\theta < 0.81$). The "good endcap" region, covering the area of $cos\theta > 0.85$, is still used for this analysis even though the resolution is slightly worse than the good barrel region. The energy resolutions for the CC are as follows:

for the barrel region,

$$\frac{\sigma_E}{E} = (\frac{0.35}{E^{0.75}} + 1.9 - 0.1E)\% \tag{3.3}$$

and for the endcap region,

$$\frac{\sigma_E}{E} = (\frac{0.26}{E} + 2.5)\% \tag{3.4}$$

for photon energies E in GeV. So photon energy resolution at 250 MeV would be 2.9% in the barrel region and 3.5% in the endcap region.

3.2.5 Superconducting Coil

The superconducting coil is essential for producing a magnetic field which curves the trajectories of the charged particles. This curvature allows the momentum of the particles to be obtained. The superconducting coil is 3.5 m in length and 2.9 m in diameter and composed of a solenoid with two layers of aluminum-stabilized superconductor. Operating at a current of 3300 amps, it produces a 1.5 Tesla axial magnetic field parallel to the beam pipe and uniform over all of the detector components mentioned above. The coil is encased in a liquid helium-filled cryostat. Just outside of the cryostat are three layers of steel which act as a magnetic field flux return for the magnet as well as a filter for the muon detectors, discussed in the next section.

3.2.6 Muon Tracking Chambers

Muons are leptons, so they do not interact strongly, and they are more massive than electrons, so they are not significantly slowed by bremsstrahlung. They are the only charged particles that can get past the flux return of the superconducting coil, making them relatively easy to identify.

Muon identification is accomplished by placing "plastic streamer counters" between several layers of iron; they are proportional counters which use a gas mixture of 50% argon and 50% ethane. These counters are 5 cm in length and 8.3 m in width, providing a spatial resolution of 2.4 cm. Outside the third layer of counters lie copper cathode strips, which provide z resolution of 2.8-5.5 cm. There are also muon chambers embedded into each endcap of the detector.

The identification of muons involves extrapolating reconstructed tracks from the tracking chambers to the muon detector. Path lengths are calculated in terms of nuclear absorption lengths. Each track is assigned a depth corresponding to the outermost level that it reaches; muon candidates are classified based on this depth.

3.2.7 Trigger and Data Acquisition

The electron and positron beams cross within the CLEO detector at a rate of 2.7 MHz; hadronic interactions from these crossings occur at about 10 Hz. At some point, it is necessary to filter out these hadronic interactions from the unwanted background crossings, which comprise most of the 2.7 MHz. The filtering process is accomplished with the trigger system, and the events are then read out of the detector using the data acquisition system (DAQ).

The trigger consisted of four levels: three hardware (L0, L1, L2) and one software (L3). The L0 trigger is the simplest, taking event information from the TOF, VD, and some from the CC in order to reduce the event rate to 20 kHz. The L1 trigger adds track counting information from the VD and DR along with CC and TOF information, taking 1 μs to further reduce the event rate to 35 Hz. The L2 trigger utilizes more sophisticated tracking information from the VD, taking 50 μs to further

decrease the event rate to 20-25 Hz. The entire detector is read out if L2 accepts an event, which takes 2 ms. Data taking is disabled while events are checked at each hardware level. If an event fails any of the first three levels, data taking is re-enabled.

The final trigger, L3, is part of the DAQ. Utilizing information from all parts of the detector, it rejects about half of the events that pass L2 while being over 99% efficient for hadronic events. This data that passes all the triggers is written to disk, then transferred to tape via the DAQ.

3.3 The CLEO II/II.V Data Sample

Two-thirds of the time, CESR runs at a center-of-mass energy of 10.58 GeV, which is the energy corresponding to the mass of the $\Upsilon(4S)$, a bound state of the b and $\bar{b}$ quarks. Approximately 25% of the events produced at this energy result in the creation of the $\Upsilon(4S)$ (see Figure 3.5); this resonance is slightly above the threshold energy necessary to produce a $B\bar{B}$ pair. The remaining 75% comprise the hadronic background for this resonance, referred to as *continuum* events, where lighter quark-antiquark pairs are produced ($u\bar{u}$, $d\bar{d}$, $s\bar{s}$, $c\bar{c}$). The other third of the time, CESR runs at an energy 60 MeV below the $\Upsilon(4S)$. This is a region where only continuum is produced (see Figure 3.5).

The data of interest for for this analysis are the continuum events containing $c\bar{c}$ pairs, collected from the CLEO II and CLEO II.V detectors. The values for the integrated luminosity are 4.7 fb^{-1} (see Appendix A) from CLEO II and 9.0 fb^{-1} from CLEO II.V. This corresponds to approximately 2×10^7 $e^+e^- \rightarrow c\bar{c}$ reactions.

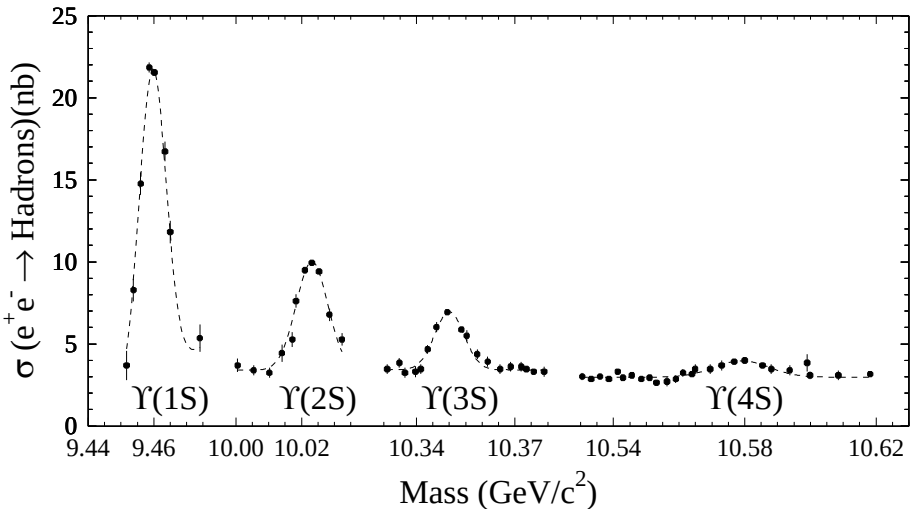

Figure 3.5: Hadronic cross section vs. center-of-mass energy. All Υ resonances are $b\bar{b}$ bound states, but only the $\Upsilon(4S)$ is massive enough to produce two B mesons.

When the data comes from the detector, it is still considered *raw* in that it is in the form of hits on individual wires, energy deposited in the calorimeter, TOF information, etc. At some point, this raw data has to be converted to tracks for which parameters such as curvature, momentum, and $\frac{dE}{dx}$ is defined. Physics analyses are conducted with the converted information, which is accomplished in a two-step process. The first step involves monitoring and simple reconstruction of the raw data using old calibration constants. Output is used to produce new calibration constants as well as diagnostic plots. The second step takes these updated constants and does a full reconstruction on the data. This data is then further condensed into the form used for analyses.

3.4 Monte Carlo (MC)

A Monte Carlo simulation refers to the production of random events based on the knowledge or predictions of the behavior of true data. For CLEO, MC refers to events that have been computer-generated based on our knowledge of the decays of various hadrons as well as the behavior of the detector. The MC is also essential for determining the acceptance, or *efficiency* of the analysis (see Sec. 6.1). It is also necessary to do MC studies before we run our analysis code over the data, since it is possible to modify selection criteria in such a way to bias the results. By working with MC first, we may obtain a set of unbiased selection criteria for applying to the data. The MC is produced in a two-step process. The first step involves creating particles which describes desired physical processes[20]. The second step takes these particles and has them produce simulated electronic signals in all of the components of the detector; this second step is accomplished using a CERN package called GEANT[21]. The output of this simulation looks exactly like the raw data obtained from the detector, so all code that is run on data (reconstruction codes, analysis code, etc) may be run exactly the same on the MC.

CHAPTER 4

Event Selection

The e^+e^- annihilation in the CLEO detector produces many different types of decay products, including $b\bar{b}$ production, lepton pair production, two photon events, cosmic rays, and $c\bar{c}$ production. Of all these sources, the only events of interest for this analysis are the $c\bar{c}$ events; even with these events, we are only interested in those pertaining to our decay modes. It is therefore necessary to define some set of criteria which will maximize the number of "interesting" events that remain and minimize the number of other events that are in the CLEO data. This chapter overviews the selection criteria for our decay modes. The cuts which define these criteria were chosen in a manner that would maximize the ratio of the number of signal events to the square root of the number of background events ($\frac{S}{\sqrt{B}}$).

4.1 Sizes of the Decay Rates

It is useful to know the size of the decay rates for our modes when attempting to develop a set of selection criteria. If we expect a small number of events for a particular mode, then we may be less inclined to use harsher cuts in favor of marginal improvements to $\frac{S}{\sqrt{B}}$.

The actual measured value returned by this analysis is a *branching ratio* (BR). The decay rate is related to the BR by the following equation:

$$BR(i) = \frac{\Gamma(i)}{\Gamma} \tag{4.1}$$

where i refers to the specific decay mode, Γ_i is the rate of decay for our meson into the specific decay mode, and Γ is the total rate of decay for our meson. This may be rewritten in terms of the lifetime, τ of the meson using the relation ($\Gamma = \frac{1}{\tau}$):

$$BR(i) = \Gamma(i)\tau. \tag{4.2}$$

The modes we are interested in are $D^+ \to \pi^+\pi^0, \bar{K}^0\pi^+, K^+\pi^0$. The first two are SCSD modes that had been previously measured by CLEO and had shown sizeable signals despite using only a fraction of the data available for this analysis. The published values for each were

$$BR(D^+ \to \pi^+\pi^0) = (2.5 \pm 0.6 \pm 0.5) \times 10^{-3} \text{ [22]} \tag{4.3}$$

and

$$BR(D^+ \to \bar{K}^0 K^+) = (7.0 \pm 1.2 \pm 0.7) \times 10^{-3} \text{ [23]}. \tag{4.4}$$

The analysis for the first mode had used 1.3 fb^{-1} and the analysis for the second had used 4.8 fb^{-1}. It was clear that using the 13.7 fb^{-1} of CLEO II and II.V would significantly improve the statistical errors on these measurements.

As for the third mode, a DCSD mode, the theoretical predictions for this decay mode were 3.7×10^{-4}[24]. To obtain a rough estimate, we may also compare $D^+ \to K^+\pi^0$ with its corresponding decay $D^0 \to K^+\pi^-$. We expect $\Gamma_{D^+\to K^+\pi^0} = \Gamma_{D^0\to K^+\pi^-}$; therefore, applying Eq. 4.2, we obtain the following relation:

$$BR(D^+ \to K^+\pi^0) = BR(D^0 \to K^+\pi^-)\frac{\tau_{D^+}}{\tau_{D^0}} \tag{4.5}$$

which gives an estimated value of 3.8×10^{-4}; we note that this is a full order of magnitude smaller than the SCSD modes, so we expect it to be at the edge of what CLEO II and II.V data could measure.

4.2 Measurement of the Branching Ratio (BR)

Using the decay mode $D^+ \to \pi^+\pi^0$ as an example, the BR for this mode is measured with the following equation:

$$BR(D^+ \to \pi^+\pi^0) = \frac{N_{D^+\to\pi^+\pi^0}}{\epsilon_{D^+\to\pi^+\pi^0} N_{D^+}} \tag{4.6}$$

where $N_{D^+\to\pi^+\pi^0}$ is raw number of events returned by our analysis, $\epsilon_{D^+\to\pi^+\pi^0}$ is the efficiency of our analysis (see Sec. 6.1), and N_{D^+} is the total number of events in our data sample that contained a D^+.

N_{D^+} is not a well known quantity, so we use *normalization* decay modes, which are modes that have relatively large and well measured BRs compared to our signal modes. For $D^+ \to \pi^+\pi^0$, we use the mode $D^+ \to K^-\pi^+\pi^+$; our measurement then becomes

$$\frac{BR(D^+ \to \pi^+\pi^0)}{BR(D^+ \to K^-\pi^+\pi^+)} = \frac{\frac{N_{D^+\to\pi^+\pi^0}}{\epsilon_{D^+\to\pi^+\pi^0}}}{\frac{N_{D^+\to K^-\pi^+\pi^+}}{\epsilon_{D^+\to K^-\pi^+\pi^+}}} \tag{4.7}$$

where the contribution from N_{D^+} has cancelled out.

$D^+ \to K^-\pi^+\pi^+$ is also the normalization mode used for $D^+ \to K^+\pi^0$. For $D^+ \to \bar{K}^0K^+$, we used $D^+ \to \bar{K}^0\pi^+$ as the normalization mode in order to reduce the systematics caused by the $\bar{K}^0$.

4.3 D^* tagging

For our analysis, we looked at two sources of D^+ mesons: those that are directly produced from the e^+e^- annihilation and those that are produced from the higher

energy resonance state D^{*+}. Within 10% errors, the cross-sections for these two sources are[25]

$$\sigma(e^+e^- \to D^+X) = 643\ pb \tag{4.8}$$

$$\sigma(e^+e^- \to D^{*+}X) = 660\ pb \tag{4.9}$$

where X means any additional decay products that may exist with the creation of the charm mesons. The BR for $D^{*+} \to D^+\pi^0$ is $(30.7 \pm 0.5)\%$, which means that the cross section for D^+s coming from D^{*+} in continuum is $(0.307 \times 660) = 202.62\ pb$. If we only accept the D^+ mesons from D^*s, then we obtain a cleaner sample (as shown in Fig. 4.1); however, it also means we are using only 25% of the total number of D^+ mesons that are available in the data sample (since we are not using the 643 pb from direct D^+ production). Nevertheless, we found that the suppression of the background was more significant than the events that were lost. We obtain D^+s from D^*s by applying a mass difference cut between the two particles; we determined the optimum cut for this was to accept all events that were within 2.5σ of the mean value of the mass difference between reconstructed D^+s and D^*s, where a σ corresponded to approximately 1 MeV.

4.4 Charged Track Selection

Each of our decay modes included one charged track in the final state (except for the normalization mode $D^+ \to K^-\pi^+\pi^+$, which has three charged tracks). All charged track candidates ($K^\pm, \pi^\pm$) were required to pass standard *track quality* cuts; these included a distance of closest approach to the beam of less than 5 mm and z value of point of closest approach to the origin of less than 5 cm. An extremely detailed discussion regarding the track quality cuts may be obtained from Ref. [26].

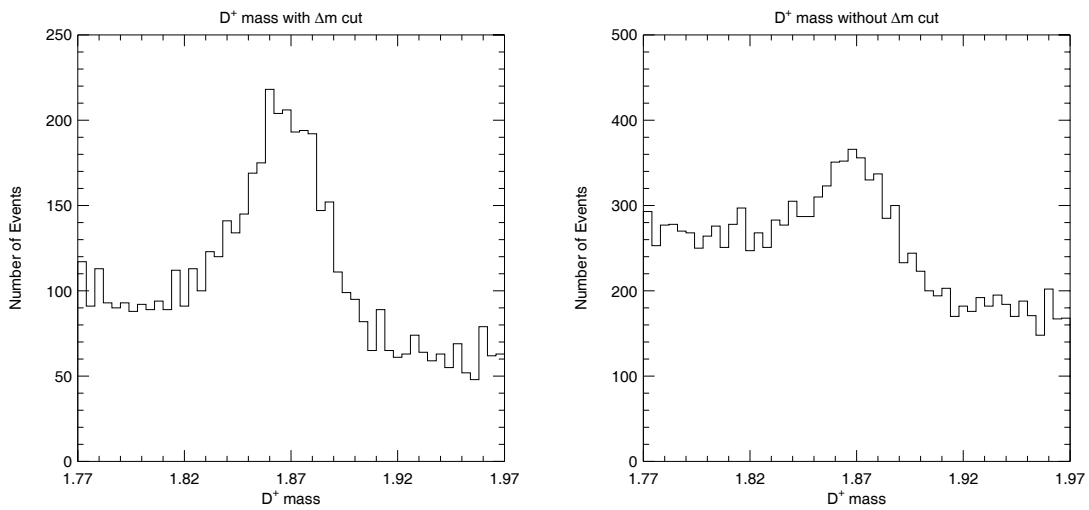

Figure 4.1: Difference in D^+ mass distribution in MC with the mass difference cut (left) and without the cut (right).

Along with the track quality cuts, tracks also had to have a momentum greater than 100 MeV; this gets rid of extremely slow tracks in the event, almost all of which are unrelated to the modes.

Finally, the tracks must pass particle identification cuts; these are defined as the normalized difference between the expected and measured values of $\frac{dE}{dx}$ for a particular particle type moving at a given momentum, or

$$SGXXDI = \frac{\frac{dE}{dx}_m^{XX}(p) - \frac{dE}{dx}_e^{XX}(p)}{\sigma_m^{XX}(p)} \tag{4.10}$$

where XX refers to the particle type (KA for $K^{\pm}$, PI for $\pi^{\pm}$, and PR for protons), p is the momentum of the particle, $\frac{dE}{dx}_m^{XX}$ is measured from the drift chamber (Sec. 3.2.2), $\frac{dE}{dx}_e^{XX}$ is its expected value, and σ_m^{XX} is the measured width of the distribution of

differences. For charged K candidates, $|SGKADI|$ had to be less than 2.0 and for charged π candidates, $|SGPIDI|$ had to be less than 3.0.

4.5 π^0 Selection

The π^0 predominantly decays into two photons (γ). In the crystal calorimeter of CLEO (Sec. 3.2.4), γs are detected. π^0s may therefore be identified by reconstructing the two γs. The π^0 candidates for this analysis were constructed by passing $\gamma\gamma$ combinations into a kinematic fitter (PI0FT3). The candidates returned by this method are those which pass the following cuts:

- $E_\gamma > 30\ MeV$ for good barrel γ
- $E_\gamma > 50\ MeV$ for bad barrel and good endcap γ
- A γ is not allowed to match with a charged track
- χ^2 on the kinematic fit of the $\gamma - \gamma$ pair had to be less than 10
- $m(\gamma\gamma)$ must be within 2.5σ of nominal π^0 mass
- $E9/E25$ cut at the 99% level.

(See Sec 3.2.4 for "good barrel" and "good endcap" descriptions). $E9/E25$ is a measure of the concentration of the shower. For π^0 candidates not directly from the D^*, we also had an additional cut of $|\vec{p}_{\pi^0}| > 250$ MeV .

4.6 K^0 Selection

Physically, it is not the K^0 meson that decays weakly, but rather, the K_S, which is a linear combination of the K^0 and $\bar{K}^0$ states. When we therefore see two πs from

a neutral K in the detector, the particle that we are reconstructing using the two πs is a K_S. The K_S candidates were obtained from a package known as *KNVF*[27]. Each K_S is reconstructed from a π^+ and a π^- track. Because we wanted to work with a very clean sample, this analysis used "gold-plated" candidates as defined by the KNVF package.

4.7 Multiple Entry Rejection

Our studies showed that we were getting multiple entries in our analysis for approximately 20% of the events. At most, we wanted only one entry per event. Therefore, for each event, we took the entry which had the lowest value of our defined χ^2:

$$\chi^2 = \frac{(\Delta M - \Delta M_{PDG})^2}{{\sigma_{\Delta M}}^2} + \sum_i \frac{(m_{\pi^0} - {m_{\gamma\gamma}}^i)^2}{{\sigma_{\pi^0}}^2} \tag{4.11}$$

where ΔM is the mass difference between the reconstructed D^* and $D^\pm$, the ΔM_{PDG} is mass difference from the PDG, and i indexes the slow π^0 and the fast π^0 for modes that include the latter. Our method of multiple entry rejection is consistent with the previous CLEO measurement for $D^+ \to \pi^+\pi^0$[22]. I also note that similar results were obtained whether or not allowing multiple entries were allowed in our yields.

4.8 Cuts on Observables

Once we obtain a sample of events that have undergone the more standard cuts, we begin to look at physical observables that will enable us to discriminate between the signal and the background. The three observables that we have selected are the mass of the reconstructed D^+ candidate, the normalized momentum of the

reconstructed D^{*+} (x_{pD^*}), and the cosine of the helicity angle ($cos\theta_{helicity}$). These observables are described in the following subsections.

4.8.1 D^+ mass

Of the three fit variables, the mass of the reconstructed D^+ gives the most clear-cut view of the signal, as seen from Fig. 4.2. It is determined by adding the four-momenta of the daughter tracks and solving for the mass:

$$m(D^+) = \sqrt{(\sum_i E_i)^2 - (\sum_i \vec{p}_i)^2} \tag{4.12}$$

where the index i goes over the daughter tracks of the D^+.

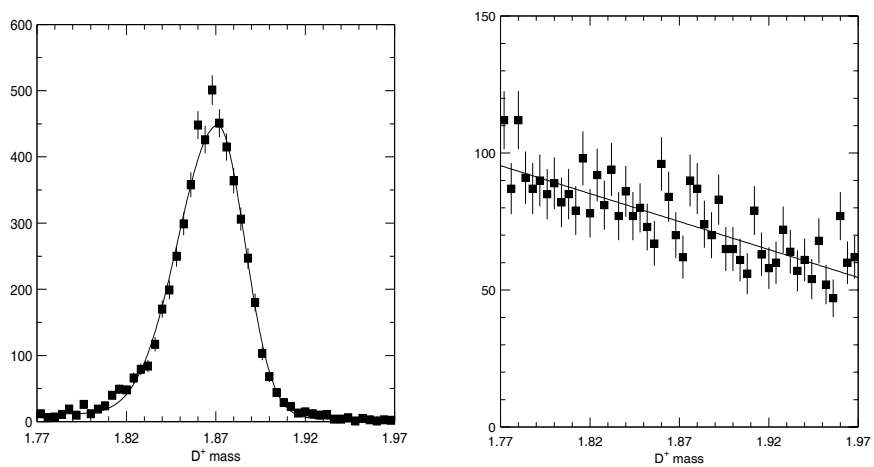

Figure 4.2: Signal (left) and Background (right) shapes for D^+ mass.

4.8.2 $x_{p_{D^*}}$

The normalized momentum of the D^*, or $x_{p_{D^*}}$, is given by the following equation:

$$x_{p_{D^*}} = \frac{|\vec{p}_{D^*}|}{\sqrt{E_{max}^2 - m_{D^*}^2}} \tag{4.13}$$

where $\vec{p_{D^*}}$ and m_{D^*} refer to the momentum and the mass of the reconstructed D^* candidate and E_{max} refers to maximum amount of energy that the D^* candidate could have possessed. This cut is useful for removing much of the random combinatoric background. I looked at removing the preselection cut on this variable in order to allow for D^+ decays from B mesons, but the $\frac{S^2}{B}$ was significantly worse if we were to do this.

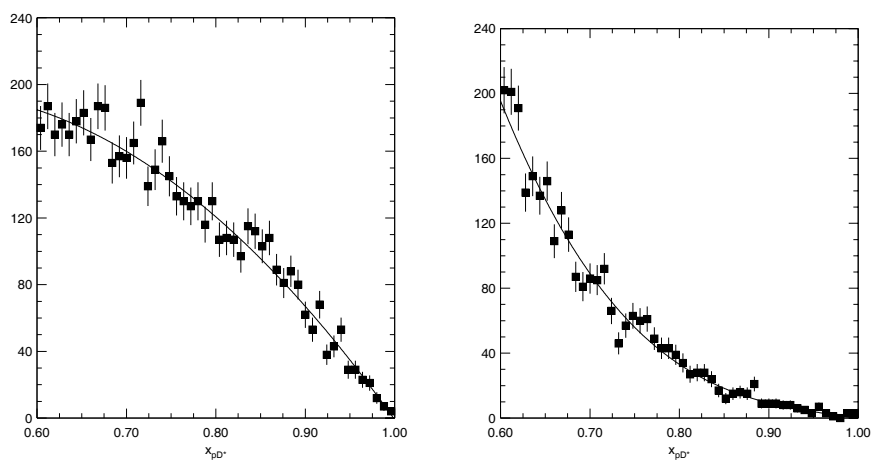

Figure 4.3: Signal (left) and Background (right) shapes for x_{pD^*}.

4.8.3 $cos\theta_{helicity}$

The $cos\theta_{helicity}$ is defined by the equation

$$cos\theta_{helicity} = \hat{p}_{K/\pi,D^+} \cdot \hat{p}_{D^+,D^*} \tag{4.14}$$

where $\hat{p}_{K/\pi}$ is the unit-vector of the momentum of the charged daughter in the rest frame of the D^+ and $\hat{p}_{D^+}$ is the unit-vector of the momentum of the D^+ in the rest frame of the D^*. This is another effective cut for removing bad D^+ candidates. The spin-0 D^+, with our spin-0 decay products, produces a flat $cos\theta_{helicity}$ distribution for our signal. Combinations of random very high or very low momentum particles cause a distribution that peaks at values of +1 and -1, respectively.

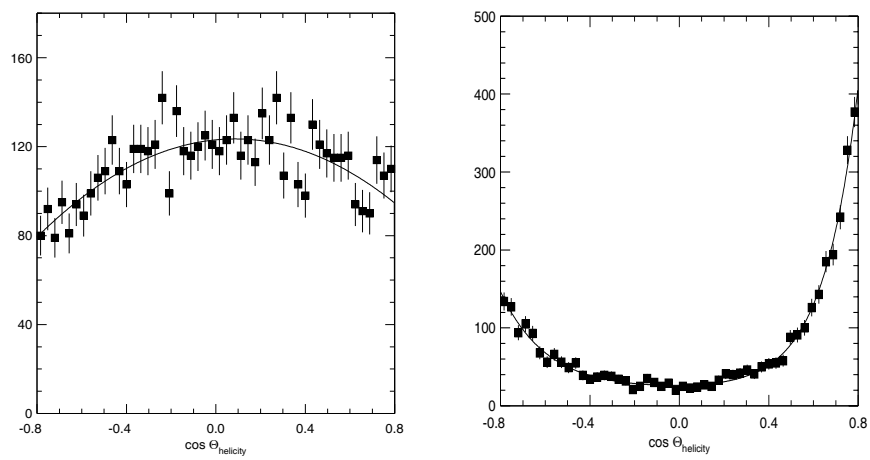

Figure 4.4: Signal (left) and Background (right) shapes for $cos\theta_{helicity}$.

4.8.4 Final Cuts

These three observables can be used to discriminate signal and background events in two ways. The first method is the more standard *cut analysis*; this involves using a single parameter to discriminate between signal and background (usually the mass of the reconstructed D^+ or the mass difference between the reconstructed D^+ and D^*), and we take advantage of the different shapes of the other observables to define cuts that will maximize $\frac{S}{\sqrt{B}}$. The drawback of this method is that once the observable is cut upon, we lose the discrimination power that exists in the overall shape differences.

The second method is the maximum likelihood method[28] which involves using all three variables in a fit, choosing slightly looser cuts and relying on shape differences to separate signal and background. For this analysis, we used the maximum likelihood method, which allows us to extract more information about each event in the dataset. Since we rely on shape differences for discrimination, we may also apply looser cuts, enabling us to obtain higher efficiencies. The final cuts used for these observables were

- mass of the reconstructed D^+ within 5σ of PDG value
- $x_{p_{D*}} > 0.6$
- $|cos\theta_{helicity}| < 0.8$.

CHAPTER 5

Maximum Likelihood Method (MLM)

In the MLM, each event is assigned a probability density function (PDF) that is related to the parameters used in the fit. The likelihood function, $\mathcal{L}$, is the product of these probability density functions for all of the events; maximizing $\mathcal{L}$ with respect to the parameters returns the values for the parameters that best describe the sample of events. The MLM is referred to as *extended* (EMLM) if it does not depend on a fixed sample size for the overall normalization of $\mathcal{L}$.

For this analysis, $\mathcal{L}$ may be written as

$$\mathcal{L}(s,b) = \frac{e^{-(s+b)}}{N!} \prod_{i=1}^{N} [s\mathcal{S}_i + b\mathcal{B}_i] \tag{5.1}$$

where N is the total number of events, s and b are the number of signal and background events, and $\mathcal{S}_i, \mathcal{B}_i$ are the PDFs for the signal and background, respectively[29]. The method of maximizing $\mathcal{L}$ involves using a CERN minimization package, MINUIT[30]. Calculating a product for a large number of events can be computationally exhaustive, so usually people will calculate the log of the likelihood function, which converts the product to a sum. Since we are using a minimization package as well, it is necessary to convert Eq. 5.1 to a function whose *minimum* will give us the best values for the parameters; this is accomplished by taking the *negative* of the log of the

likelihood function, or

$$-2log\mathcal{L} = 2(s+b) + 2N! - 2\sum_{i=1}^{N} log[s\mathcal{S}_i + b\mathcal{B}_i]. \tag{5.2}$$

The implementation of this method is encoded into a fitting program called FELIX[31]. FELIX, designed by Vladimir Savinov, allows a user to specify PDFs for an arbitrary number of observables, run over a given sample of data, interface with MINUIT, and obtain the number of signal and background events (s, b) as defined by the EMLM.

It should be noted that the PDFs, $\mathcal{S}_i$ and $\mathcal{B}_i$, may be combinations of PDFs from several observables. For this analysis, three observables were used: D^+ mass, $x_{p_{D^*}}$, and $cos\theta_{helicity}$. $\mathcal{S}_i$ and $\mathcal{B}_i$ may therefore be rewritten as $\mathcal{S}_i = \mathcal{S}_i^{D^+mass}\mathcal{S}_i^{x_{pD^*}}\mathcal{S}_i^{cos\theta helicity}$ and $\mathcal{B}_i = \mathcal{B}_i^{D^+mass}\mathcal{B}_i^{x_{pD^*}}\mathcal{B}_i^{cos\theta helicity}$, where $\mathcal{S}_i^X$ and $\mathcal{B}_i^X$ refer to the PDF shapes of observable X for signal and background, respectively. The following sections give our method for determining the PDFs for the events describing the signal and background of these observables.

5.1 Description of PDF Shapes

For the signal shapes, we generated signal MC for each decay mode; with the MC, we plotted the distributions for our three variables. Each distribution was then fit to a function which described the PDF for this variable. The resulting signal PDFs are shown in Figures 5.4-5.12. For the background shapes, the CLEO generic MC for our signal described the data well for everything but the $x_{p_{D^*}}$ distribution. At the time of this note, the default setting for the control files for generating MC, as well as the generic MC on the staged tapes, had a systematic error with regards to the x_p distribution: it would generate D^* particles with softer momenta than

that which the data exhibited. Fortunately, a correction to the control file was determined[32], and we were able to correct the shape of the signal MC. Creating a corrected background sample, however, would have taken an overwhelming amount of CPU and disk space. Using the actual data from the sideband region outside of our defined D^+ mass window (referred to as *sideband data*), a shape for the x_p could be created which would describe the background. The resulting background PDFs for each mode are shown in Figures 5.5-5.13.

To use a consistent sample for our background PDFs, using the sideband data for all three variables was considered. However, we were unable to do so for the D^+ mass because the way the signal is defined: only D^+ mesons that come from a D^{*+} meson were included. As a result, there is a small amount of D^+ mesons which peak in our signal region which come directly from the e^+e^- annihilation and not from a D^*; such events were chosen to be classified as background. For this reason, the generic MC had to be used to determine this background shape.

For different reasons, the sideband data was unusable for determining the $cos\theta_{helicity}$ PDF: the shape of this variable changes for high and low sideband D^+ mass regions as seen in Fig 5.2. Because of this, there is a slight discrepancy between the anti-tagged MC in the signal region and the sideband MC (Fig 5.3). This ruled out the possibility of using the sideband data.

Another problem encountered was they mysterious peak for the background shape of the $cos\theta_{helicity}$ for $D^+ \rightarrow K_S\pi^+$ (See Fig. 5.11). We were able to find that this was caused by $D_S^+ \rightarrow K^+K_S$ being misidentified as our signal. The effects of removing these events are shown in Figure 5.1. Fortunately, this mode is dominated by the signal rather than the background, so we determined that fitting the

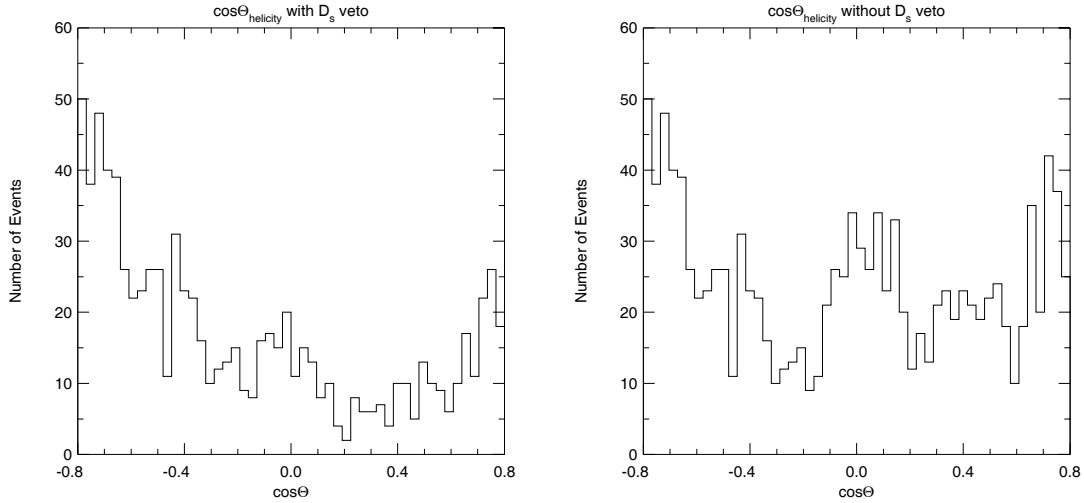

Figure 5.1: Comparison of $cos\theta_{helicity}$ for MC with a veto on $D_S \rightarrow K^+K_S$ (left) and without (right).

PDF to a function that did not include the bump changed our resulting BR by less than a 0.1 σ. Since it was so insignificant, we did not need to correct for it.

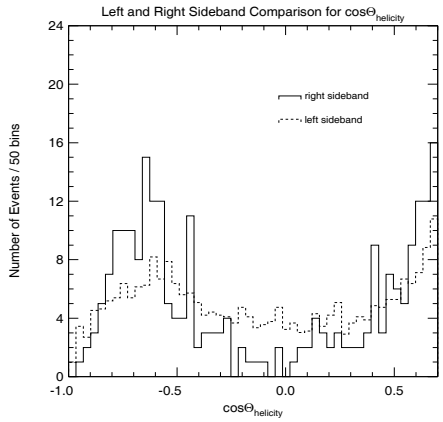

Figure 5.2: Comparison of $cos\theta_{helicity}$ for the left and right sideband regions of the generic anti-tagged MC of $D^+ \rightarrow K^+\pi^0$

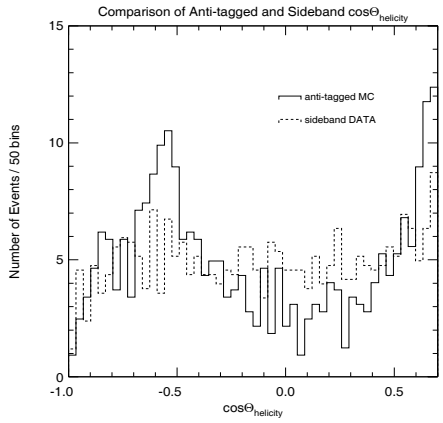

Figure 5.3: Comparison of $cos\theta_{helicity}$ for generic anti-tagged MC and sideband MC of $D^+ \rightarrow K^+\pi^0$

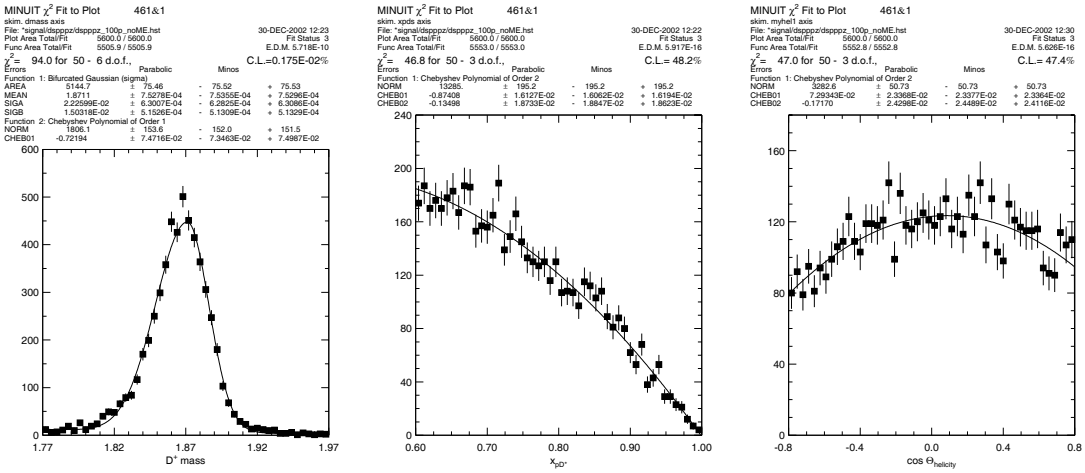

Figure 5.4: PDF for Signal $D^+ \to \pi^+\pi^0$

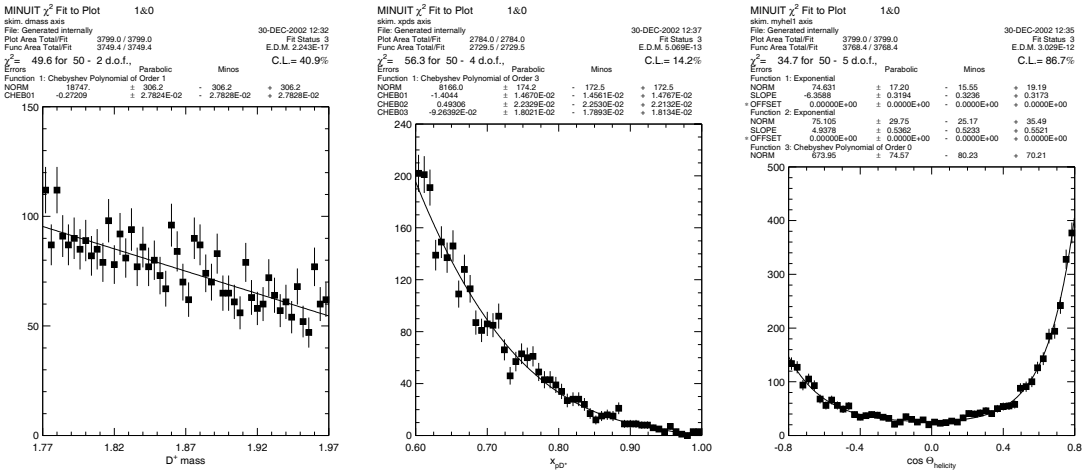

Figure 5.5: PDF for Background $D^+ \to \pi^+\pi^0$

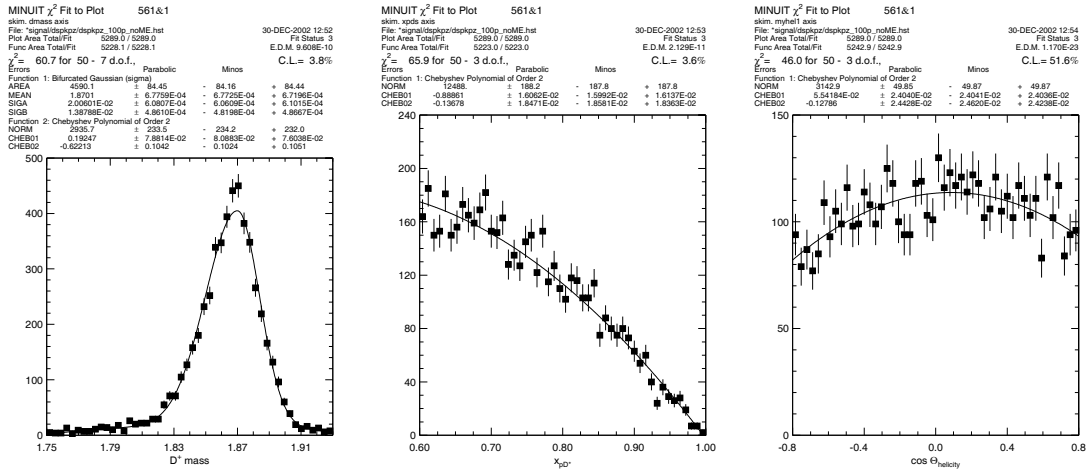

Figure 5.6: PDF for Signal $D^+ \to K^+\pi^0$

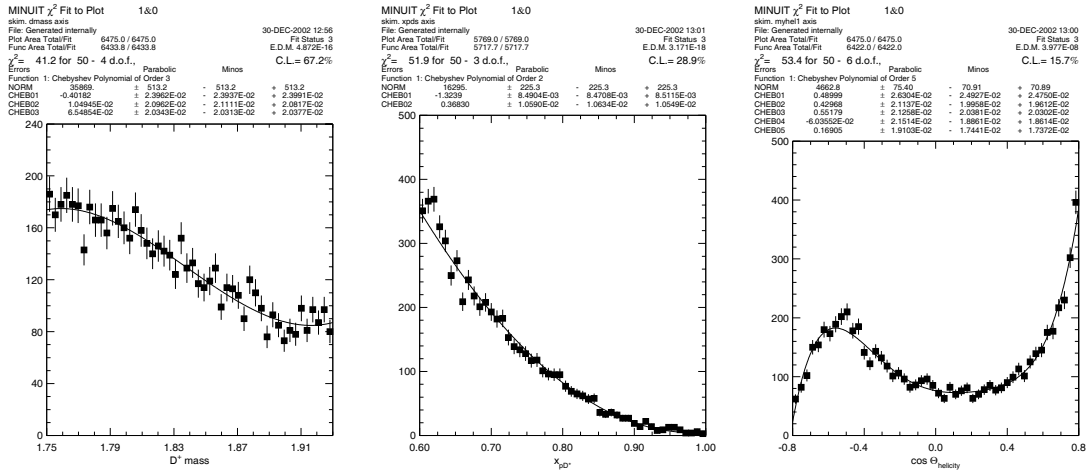

Figure 5.7: PDF for Background $D^+ \to K^+\pi^0$

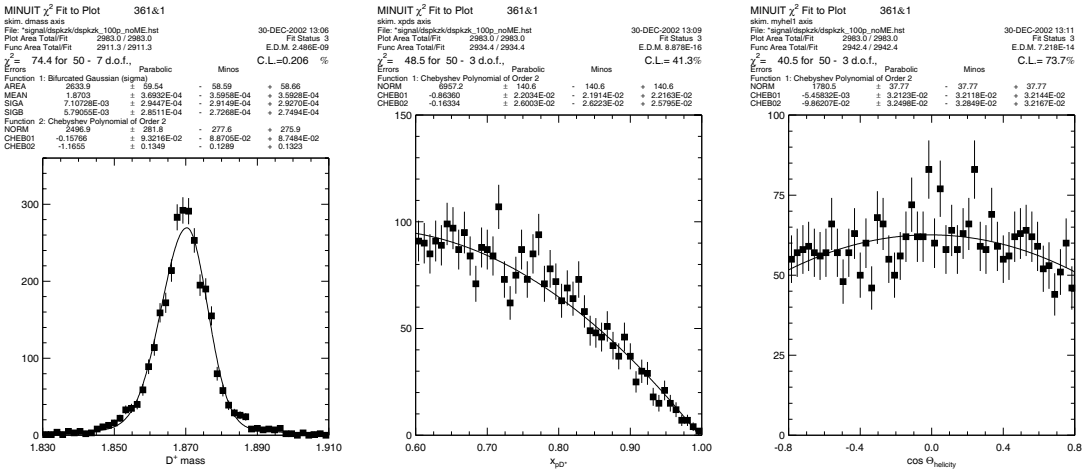

Figure 5.8: PDFs for Signal $D^+ \to K^+ K_s$

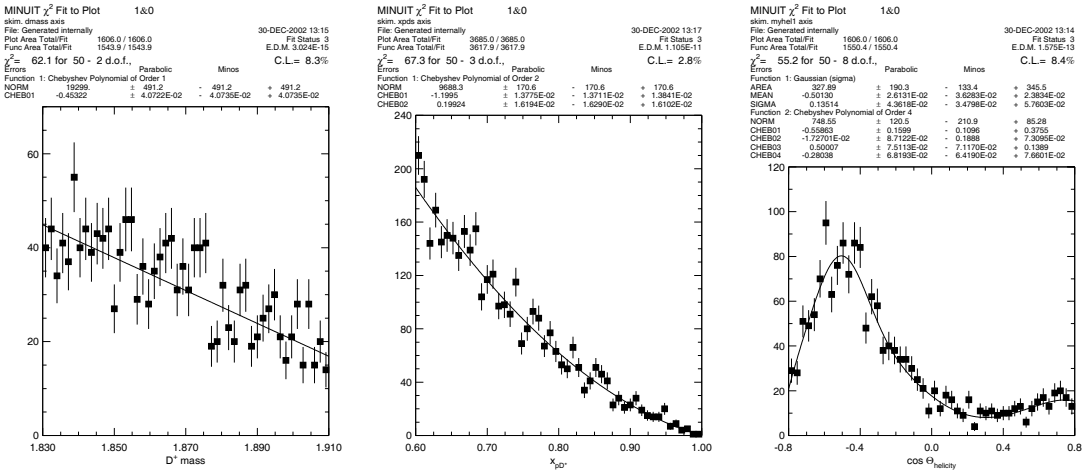

Figure 5.9: PDFs for Background $D^+ \to K^+ K_s$

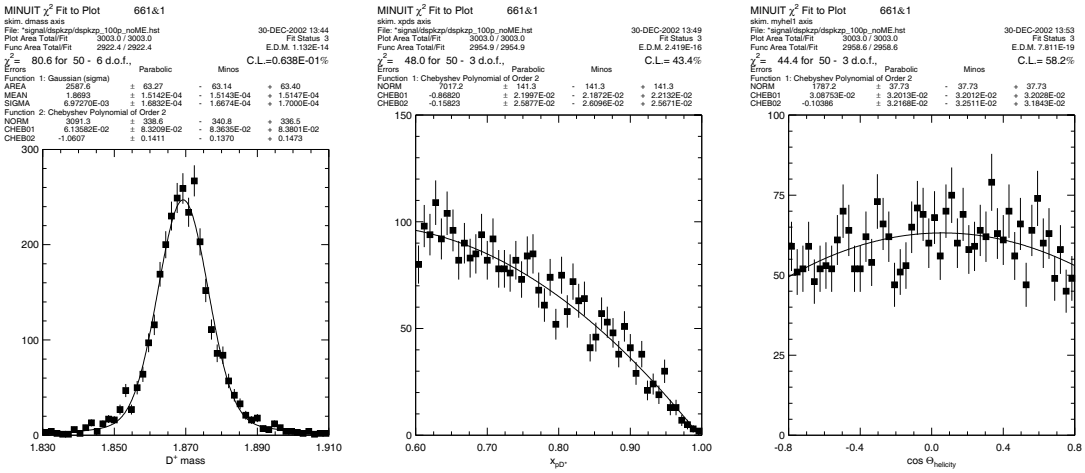

Figure 5.10: PDFs for Signal $D^+ \to \pi^+ K_s$

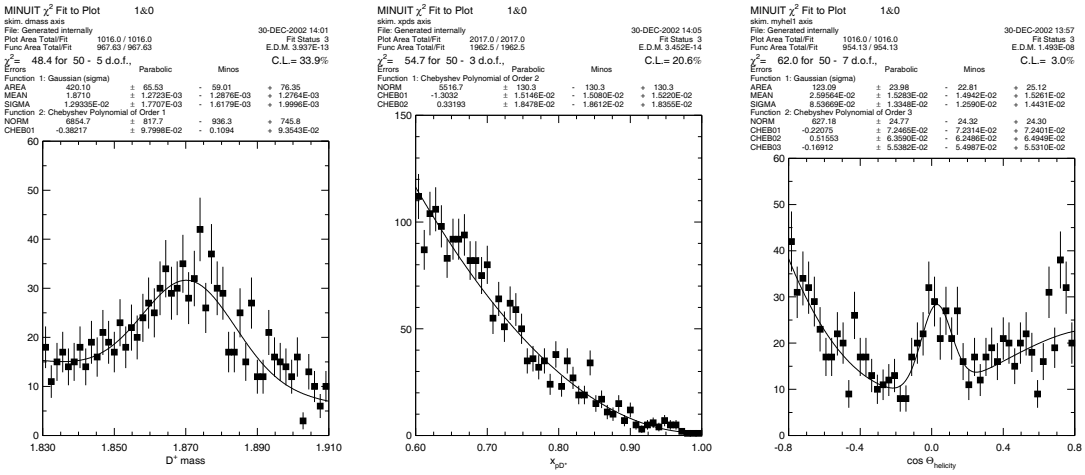

Figure 5.11: PDFs for Background $D^+ \to \pi^+ K_s$

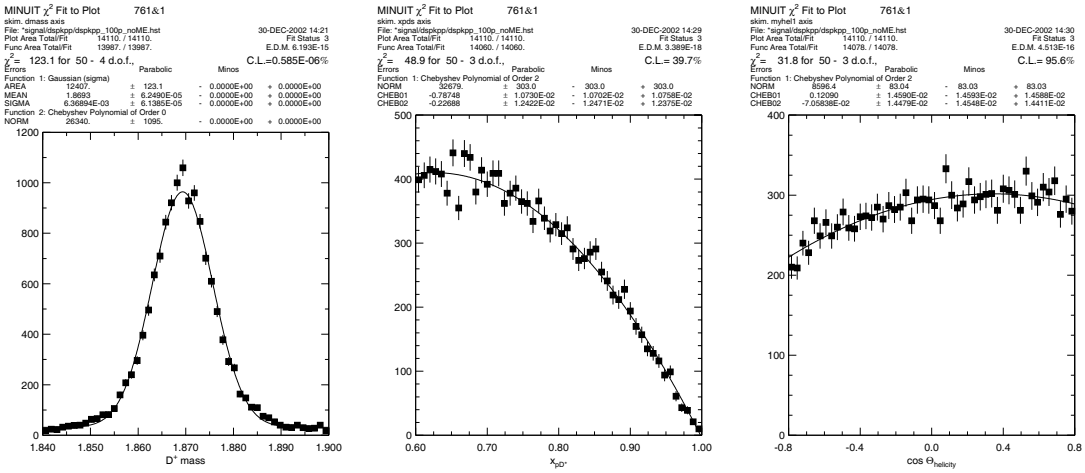

Figure 5.12: PDFs for Signal $D^+ \to K^-\pi^+\pi^+$

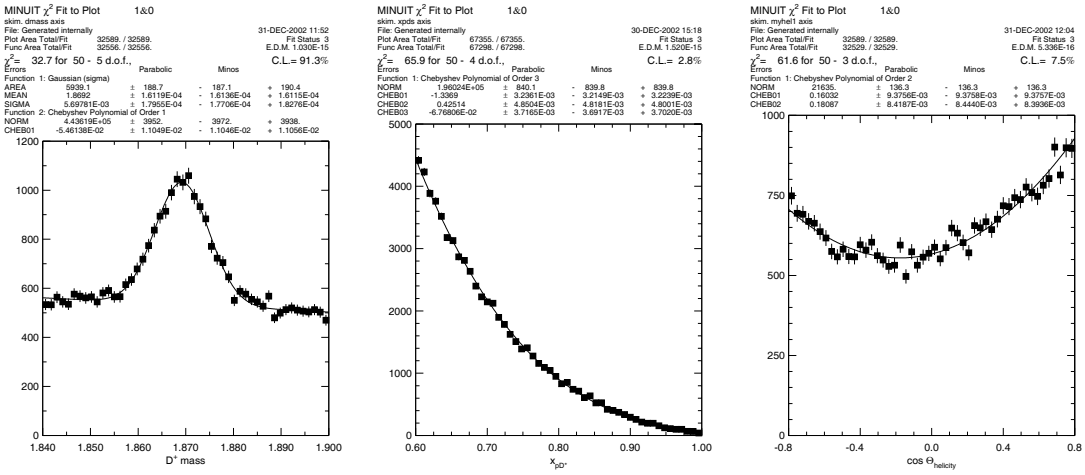

Figure 5.13: PDFs for Background $D^+ \to K^-\pi^+\pi^+$

CHAPTER 6

Results and Discussion

> The results of the experiment were inconclusive, so we had to use statistics. –*Unknown*

To begin, I present the equation used for converting our measurements to a branching ratio, or in this case, a ratio of branching ratios since a normalization mode is used for each signal mode:

$$\frac{BR(Signal)}{BR(Normalization)} = \frac{\frac{yield(Signal)}{\epsilon(Signal)}}{\frac{yield(Normalization)}{\epsilon(Normalization)}} \tag{6.1}$$

where the yield refers to the raw yields returned by the fitter, given in Table 6.1, and ϵ refers to the efficiencies from Table 6.2. To obtain our final result, we will calculate Eq. 6.1 for each of our modes, and list two errors: the first is a statistical error that is returned by our fitter and the second is a systematic error encompassing all other errors that are not statistical in nature. This chapter will present our method for calculating efficiency, the determination of the systematic errors, and the final results.

6.1 Efficiency

As mentioned in Ch. 4, selection criteria are applied to maximize the $\frac{S}{\sqrt{B}}$. In applying these criteria, it is inevitable that events containing the signal modes will

Signal Mode	Raw Yield
$\pi^+\pi^0$	171.32 ± 22.07
$K^+\pi^0$	34.31 ± 20.88
K^+K_S	277.70 ± 20.76
Normalization Mode	**Raw Yield**
$K^-\pi^+\pi^+$	$12898. \pm 156.61$
π^+K_S	1434.7 ± 48.03

Table 6.1: Raw Yields from CLEO II and II.V data using FELIX

be lost. The efficiency of the analysis refers to the fraction of the number of signal events that remain after they are passed through the selection criteria and the fitter.

To calculate the efficiency, MC events were used, since the MC allows us to know exactly how many signal events we started with. Variable amounts of signal MC events were taken and combined it with a constant number of generic background MC events, consistent with that expected from the data yield. Each combination of signal and background underwent the cuts defined in Ch. 4 before being passed through the fitter; the fitter would then output a value for the number of signal events that it found in the sample. These output yields were plotted versus the corresponding number of input signal MC events in the sample before *ANY* cuts were applied; these plots were each fit to a straight line, whose slope determined the efficiency of this analysis. The linear fits may be seen in Figures 6.1 and 6.2. The offset is the output yield for no input MC events; ideally, we expect this to be as close to zero as possible. If it is large, then it will introduce a bias in the yield, but fortunately for our modes, the offsets are all negligible. The error on the offset of $D^+ \to K^-\pi^+\pi^+$ is large, but since this is a normalization mode whose yield from

Signal Mode	Efficiency	Offset
$\pi^+\pi^0$	$(6.20 \pm 0.11)\%$	-2.87 ± 10.21
$K^+\pi^0$	$(6.08 \pm 0.22)\%$	-2.87 ± 6.43
K^+K_s	$(3.44 \pm 0.04)\%$	4.26 ± 8.66
Normalization Mode	**Efficiency**	**Offset**
$K^-\pi^+\pi^+$	$(6.74 \pm 0.12)\%$	-1.85 ± 123.76
π^+K_s	$(3.33 \pm 0.06)\%$	-1.35 ± 19.28

Table 6.2: Reconstruction Efficiencies and Offsets from MC

the data is on the order of 10^5, this large error still proves to be negligible in the calculation of our final result.

6.2 Systematic Errors

The systematic errors refer to the errors that are not dependent on the number of events in a given sample; ie, that are not statistical in nature, such as errors introduced by track finding efficiency. This section defines the sources of systematic error for this analysis, as well as their calculation. The sources that were taken into consideration include

- 1% for each charged track[33], added linearly. This systematic is caused by the uncertainty in the MC's ability to describe the data accurately when applying track finding/reconstruction programs. All of the signal modes have one charged track; one of the normalization modes ($K^-\pi^+\pi^+$) has three charged tracks and the other ($K_S\pi^+$) has only one. Since we are measuring the quotient of BRs, the systematic will be the difference in the number of charged tracks

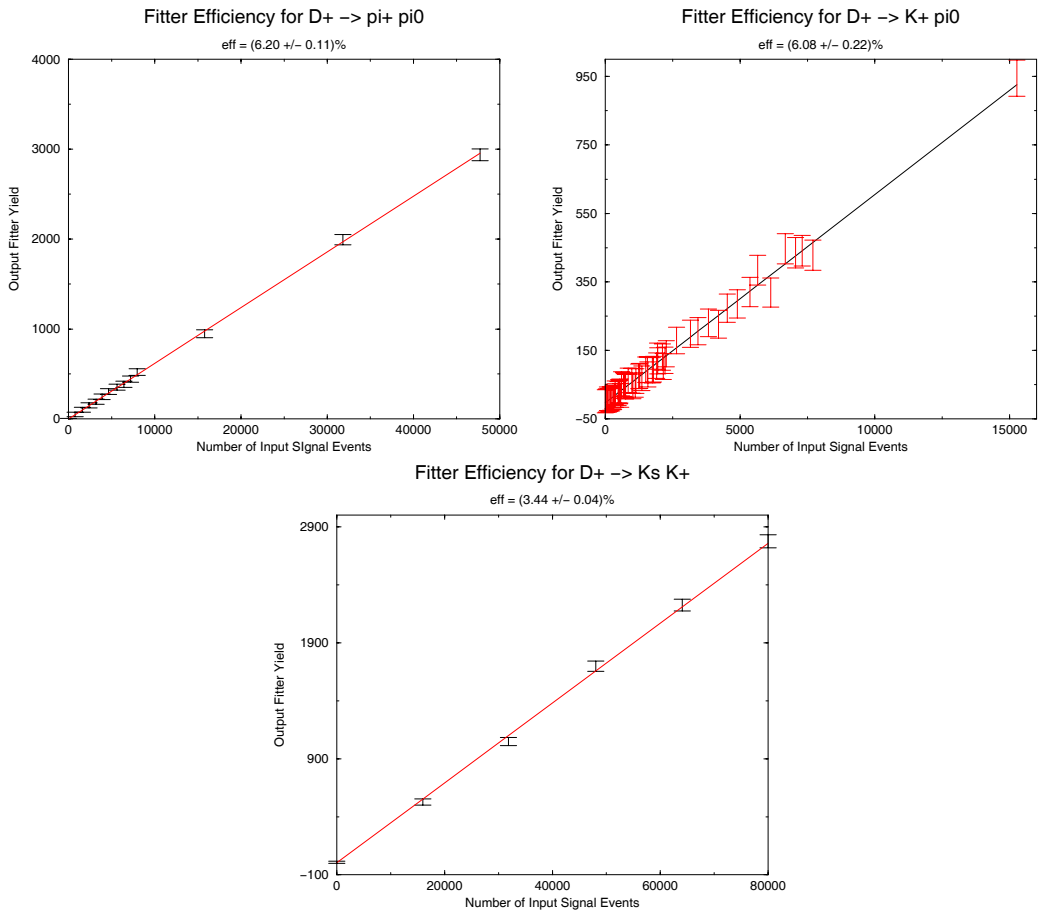

Figure 6.1: Efficiency Fit for Signal Modes

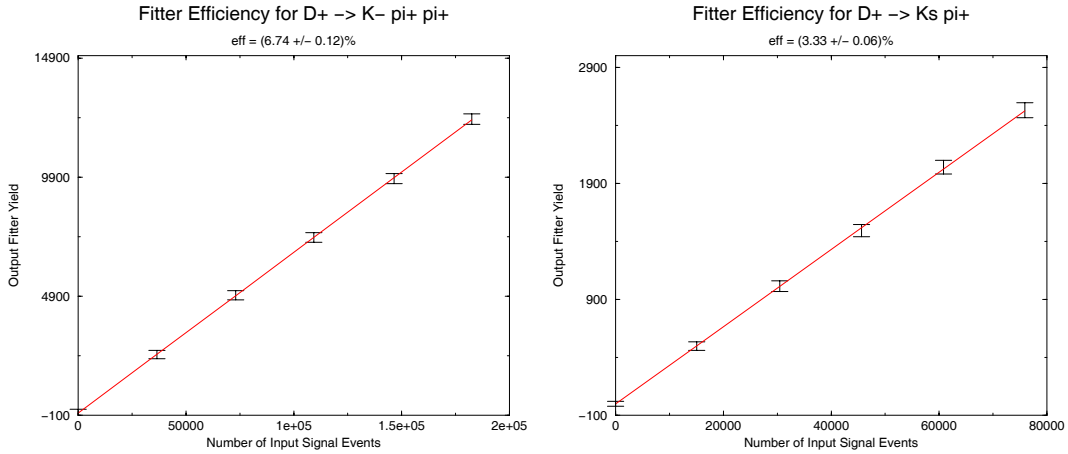

Figure 6.2: Efficiency Fit for Normalization Modes

of a signal mode and the normalization mode. For $\pi^+\pi^0$ and $K^+\pi^0$, the contribution from this source is 2% and for $K_S K^+$, the contribution completely cancels.

- 5% from finding efficiency for π^0 candidates. This is also an error introduced by uncertainty in the ability of the MC to correctly take two photons and reconstruct the π^0 from them. Only fast π^0 are considered because the contribution of slow π^0 cancels since there is a slow π^0 in the signal and normalization mode for each measurement. Therefore this systematic is only included for the $\pi^+\pi^0$ and $K^+\pi^0$ measurements.

- Uncertainty from efficiency calculation contributes between 1% and 2.2%. The values for each mode can be obtained from Table 6.2. Offsets were negligible, so these effects were ignored.

- Errors from PDF parameterization, listed in Table 6.3. The parameters describing the shapes on the PDFs each have a corresponding error returned by the minimization program. Our systematic study on the PDF shapes, discussed in the following section, shows the uncertainty in our measurements caused by the errors in our shape parameters.

The first three systematic errors are standard for CLEO analyses. The last source, the PDF parameterization, turned out to be the largest by far. A description of this source follows in the next section.

6.2.1 Systematic Error on PDF shapes

To determine the systematic error for each mode, we modified all of the parameters simultaneously using Gaussian distributed random numbers. The sigmas for the random numbers were taken from the MINOS errors for each parameter. The data was then refit, using FELIX, with the newly defined PDF shapes. We repeated this process many times and looked at the distribution of yields returned from the fitter. The distribution of yields for each mode was fit to a Gaussian function, and we defined our systematic error for the PDFs as the 1σ error returned by the Gaussian fit.

Signal Mode	Systematic Error
$\pi^+\pi^0$	4.7%
$K^+\pi^0$	31.1%
K^+K_s	2.6%
Normalization Mode	**Systematic Error**
$K^-\pi^+\pi^+$	0.5%
π^+K_s	2.8%

Table 6.3: Systematic Errors from PDF shapes. The raw event yields returned from FELIX, along with the statistical errors, are given in the second column as a source of comparison for the systematic errors listed in the third column.

As a cross-check, we also calculated the systematic error using an alternate method[34]. This involves varying one parameter at a time between refits rather than varying them all simultaneously. Also, we modified the parameters by a full positive and negative sigma rather than using Gaussian distributed random numbers. The sigmas were again obtained from the MINOS errors on each parameter. This method

was not only very consistent with the systematic errors returned by our method, but it was also useful in determining which shapes were predominantly responsible for the size of the systematic errors.

Our studies showed that the x_{pD^*} shape was the largest cause of the systematic errors for our modes. As a final study, we saw if there were any correlations in the parameters of this PDF, since the existence of correlations would invalidate our approach to determining the systematic error. The $x_{p_{D^*}}$ background PDF is defined with a second order Chebyshev polynomial. When fitting this shape with MINUIT, there are three parameters: NORM, CHEB01, and CHEB02. To study the correlation of the parameters, we varied the number of events in each bin of our $x_{p_{D^*}}$ histogram using a Poisson distributed random number. We then used MINUIT to refit our histogram to obtain values for each of our three parameters. We repeated this process 1000 times and then used Eq. 6.2 on two of the parameters at a time.

$$V_{xy} = \frac{\overline{xy} - \bar{x}\bar{y}}{\sqrt{(\overline{x^2} - \bar{x}^2)(\overline{y^2} - \bar{y}^2)}} \tag{6.2}$$

For highly correlated (or anti-correlated) parameters, we would expect to have a value of 1 (or -1) for V_{xy}. The results from Table 6.4 shows that there is a negligible amount of correlation between these parameters.

Parameters	V_{xy}
NORM, CHEB01	-4.31×10^{-4}
NORM, CHEB02	4.32×10^{-4}
CHEB01, CHEB02	-1.86×10^{-7}

Table 6.4: Correlations of parameters on $x_{p_{D^*}}$ background shape

6.3 Final Results

Using Eq. 6.1, along with the results from Tables 6.1 and 6.2 and the systematic contributions from Sec. 6.2, our final results are

$$\frac{BR(D^+ \to \pi^+\pi^0)}{BR(D^+ \to K^-\pi^+\pi^+)} = 0.0144 \pm 0.0019 \pm 0.0010 \tag{6.3}$$

$$\frac{BR(D^+ \to K^+\pi^0)}{BR(D^+ \to K^-\pi^+\pi^+)} = 0.0029 \pm 0.0018 \pm 0.0009 \tag{6.4}$$

$$\frac{BR(D^+ \to K^+K_S)}{BR(D^+ \to \pi^+K_S)} = 0.1874 \pm 0.0153 \pm 0.0085. \tag{6.5}$$

Using the values of the normalization modes from the PDG[2], the absolute branching ratios for the three signal modes are

$$BR(D^+ \to \pi^+\pi^0) = (1.3 \pm 0.2) \times 10^{-3} \tag{6.6}$$

$$BR(D^+ \to K^+\pi^0) = (2.6 \pm 1.8) \times 10^{-4} \tag{6.7}$$

$$BR(D^+ \to K^+K_S) = (5.2 \pm 0.6) \times 10^{-3} \tag{6.8}$$

where the statistical and systematic errors for our measurements have been combined in quadrature.

The result for $D^+ \to \pi^+\pi^0$, given in Eq. 6.3 was a bit surprising, since the previous CLEO measurement[22] had been

$$\frac{BR(D^+ \to \pi^+\pi^0)}{BR(D^+ \to K^-\pi^+\pi^+)} = 0.028 \pm 0.006 \pm 0.005. \tag{6.9}$$

At first glance, this would seem alarming, since our result is half of this result from 1993! At second glance, we note that it is only about 2.3σ larger than the result from this analysis, which is large, but does not seem as drastic as the first glance indicated. Since there was this disagreement, cross-checks were conducted

(Appendix C) in the form of a cut analysis to not only reproduce the previous CLEO measurement (which used only the 4s2 and 4s3 precompress data sets), but also to confirm our result when using the entire CLEO II and II.V data sets. As an additional note, our new result confirms $SU(3)_F$ predictions (Sec. 8.1), whereas the previous result had disagreed.

The result for $D^+ \to K_S K^+$ proved consistent with previous measurements from CLEO[23] and FOCUS[35]:

- CLEO 1997: $\frac{BR(D^+ \to K^+ K_S)}{BR(D^+ \to \pi^+ K_S)} = (22.2 \pm 4.1 \pm 1.9)\%$.
- FOCUS 2002: $\frac{BR(D^+ \to K^+ K_S)}{BR(D^+ \to \pi^+ K_S)} = (19.96 \pm 1.19 \pm 0.96)\%$.

The DCSD mode $D^+ \to K^+ \pi^0$, which began as the focus of the analysis, only returned a 1.6σ result; a subsequent $SU(3)_F$ calculation in Sec. 8.1 shows that this is approximately the number of events expected from the data set. As a result, an upper limit would have to be calculated for this mode. Sec. 7 reviews the method used to obtain this limit.

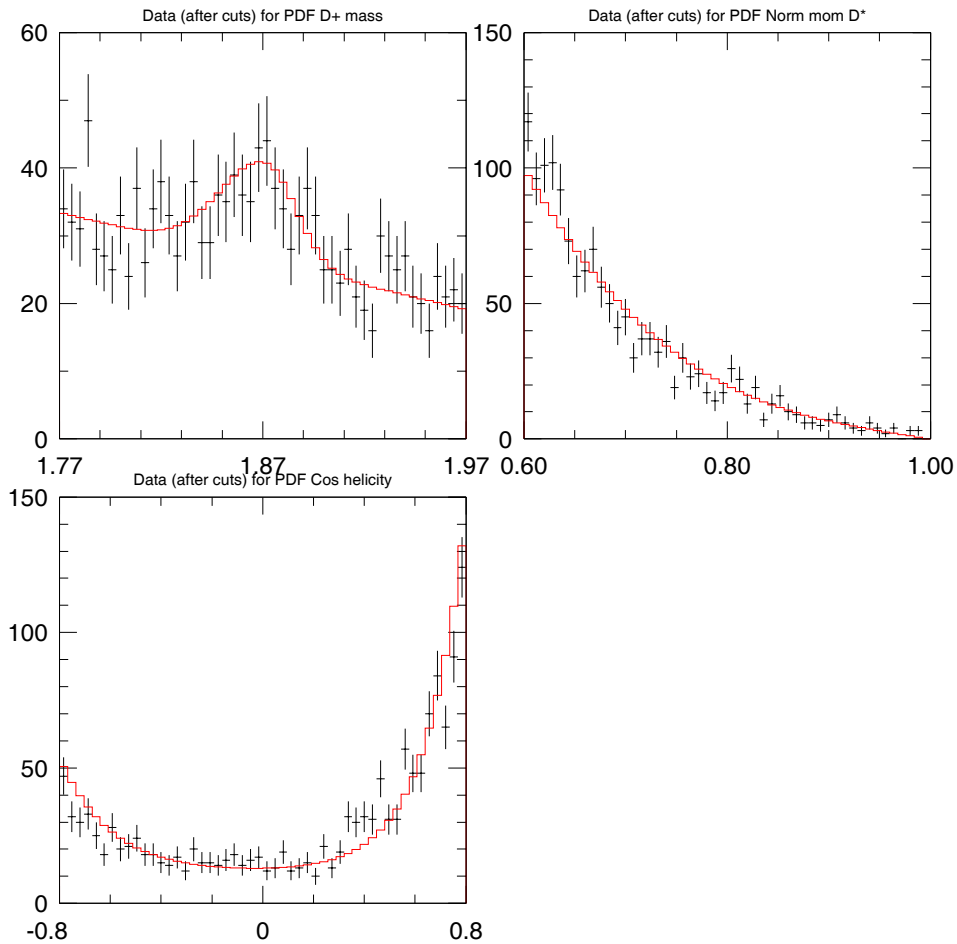

Figure 6.3: Fit Variables for $D^+ \to \pi^+\pi^0$. The points are from CLEO II and II.V data (with error bars) and the red solid line is the fit from FELIX

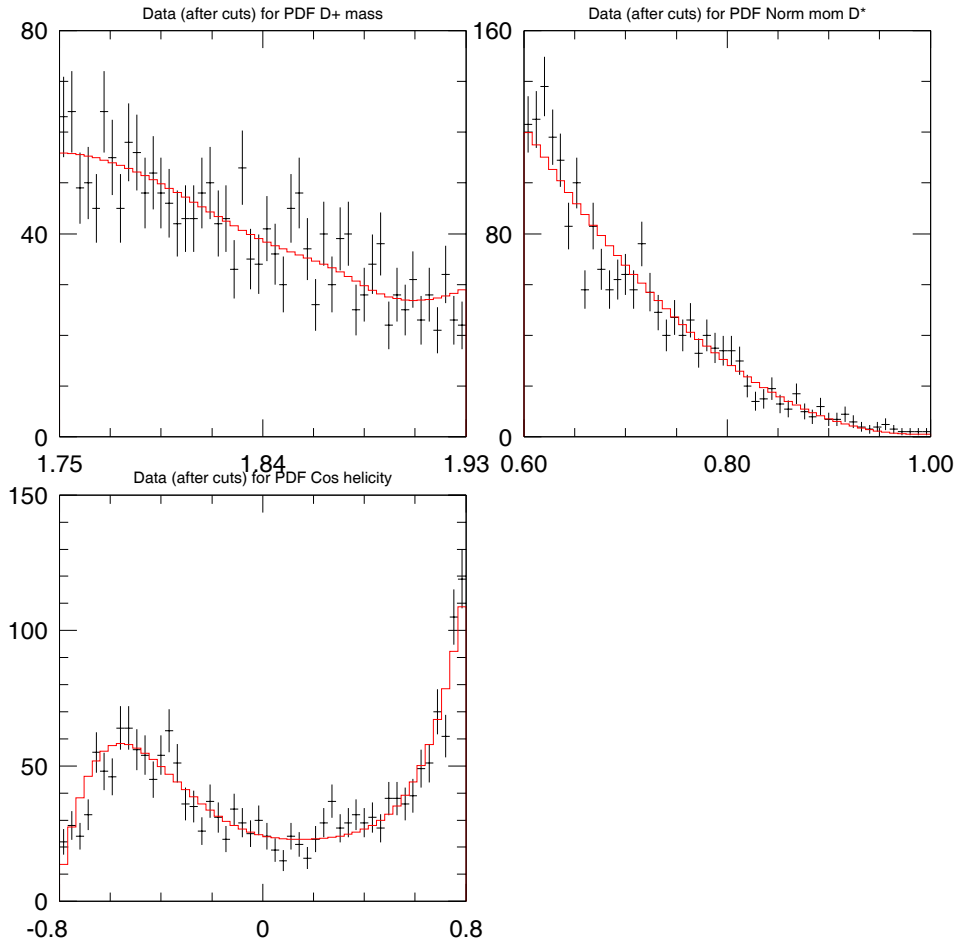

Figure 6.4: Fit Variables for $D^+ \to K^+\pi^0$. The points are from CLEO II and II.V data (with error bars) and the red solid line is the fit from FELIX

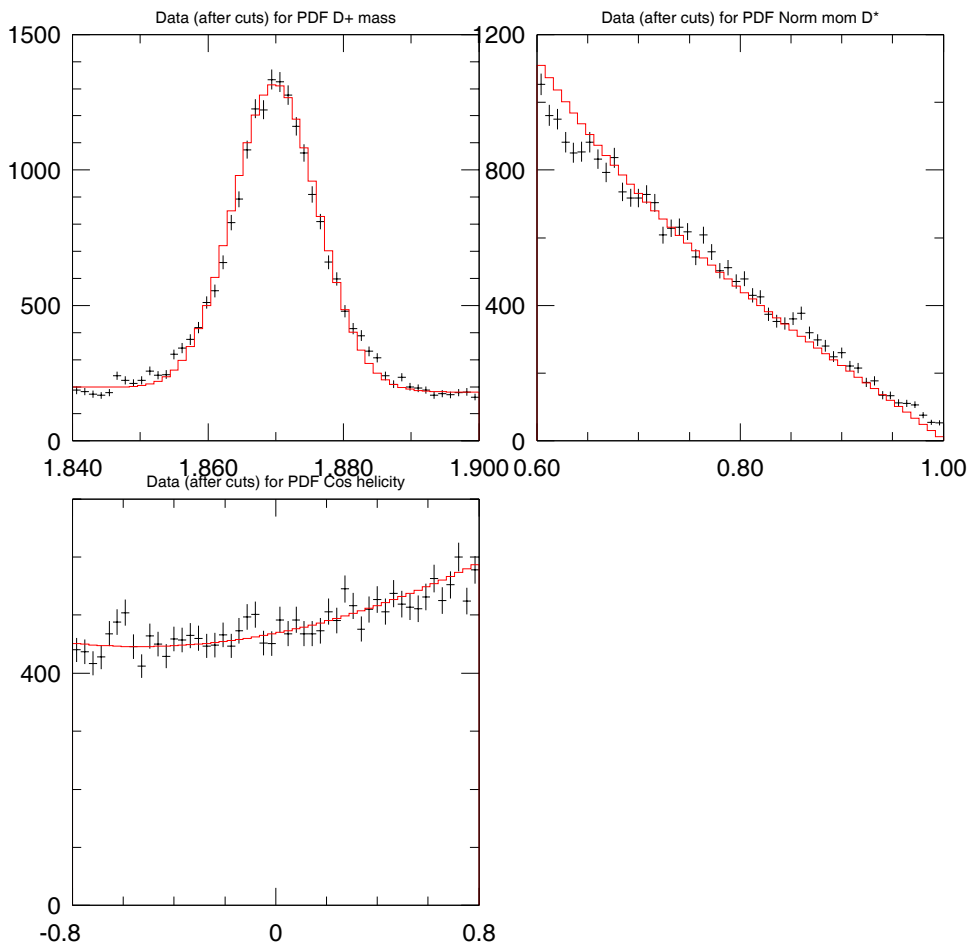

Figure 6.5: Fit Variables for $D^+ \to K^-\pi^+\pi^+$. The points are from CLEO II and II.V data (with error bars) and the red solid line is the fit from FELIX

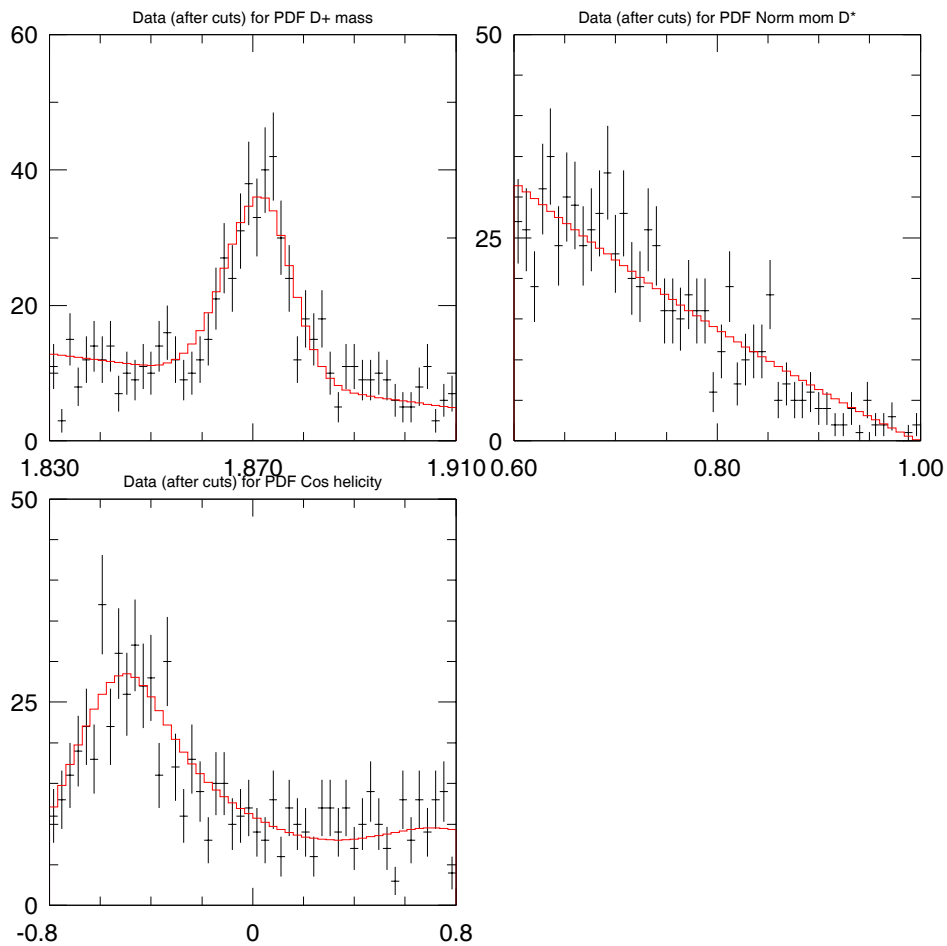

Figure 6.6: Fit Variables for $D^+ \to K^+ K_s$. The points are from CLEO II and II.V data (with error bars) and the red solid line is the fit from FELIX

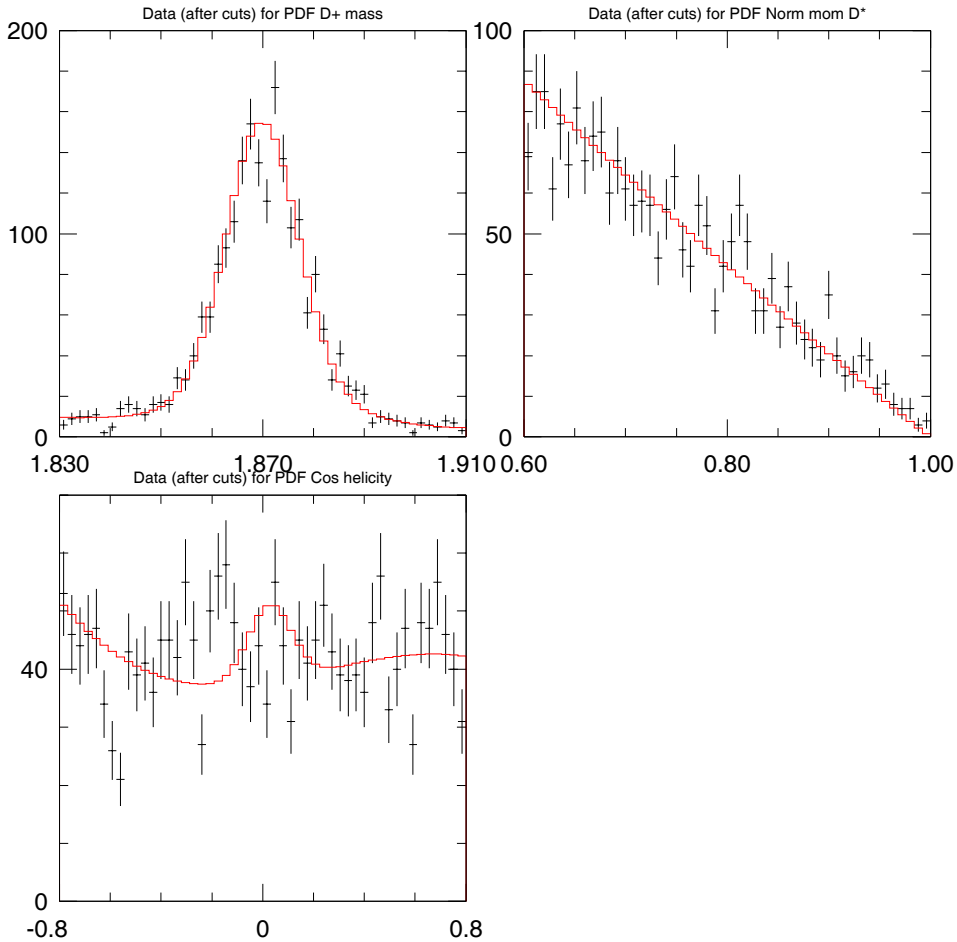

Figure 6.7: Fit Variables for $D^+ \to \pi^+ K_s$. The points are from CLEO II and II.V data (with error bars) and the red solid line is the fit from FELIX

CHAPTER 7

Obtaining Upper Limit for $D^+ \to K^+\pi^0$

> If you went to Vegas and have a 99% chance of winning, you'd bet the house! –*Richard Kass*

It is traditionally accepted among particle physicists that a 3σ signal (corresponding to a 99% probability in a gaussian distribution that a measurement is correct) is the lowest significance that a true signal will exhibit. Our result of

$$\frac{BR(D^+ \to K^+\pi^0)}{BR(D^+ \to K^-\pi^+\pi^+)} = 0.0029 \pm 0.0018 \pm 0.0009 \tag{7.1}$$

corresponds to 1.6σ, which is about an 89% probability. This is not considered significant enough to "bet the house". We therefore determined a 90% confidence level (C.L.) upper limit for this decay mode; for a Gaussian distribution, this is the value, x, for $BR(D^+ \to K^+\pi^0)$ where the integrated area from $-\infty$ to x is 90% of the total area of the gaussian distribution. This is also typically assumed to be the value at which we would have seen a signal if the BR were equal to the upper limit. Ideally, to determine the upper limit, we would create 1000 MC samples, equal in size to our data sample, using the procedure in Sec. 3.4. We could then run our analysis code over these samples and obtain 1000 yields to determine our

upper limit. Unfortunately, to produce this much MC would have taken too much computing time and disk space.

To conduct this study, however, we do not need all the track information, but rather, only values for the three observables. Since we know the distribution for the signal and background shapes for each observable, and since we found the observables to be uncorrelated, we could produce new "datasets" by creating randomly generated values for D^+ mass, x_{pD^*}, and $\cos\theta_{helicity}$ based on the PDFs. This would also take significantly less computing time and disk space than our other option of producing CLEO MC.

We also included systematic errors in our upper limit calculation. Since the error caused by the PDF definitions (31%) was significantly larger than all of the other sources (5.6%), we only used the former in our upper limit calculation. For each of our new data sets, we varied the PDFs systematically 40 times, refitting after each variation.

After obtaining a list of yields from this procedure, we fit the distribution to a Gaussian and determined the 90% C.L. We determined this to be 57.20

Using values from Tables 6.2 and 6.1, our upper limit is

$$\frac{BR(D^+ \to K^+\pi^0)}{BR(D^+ \to K^-\pi^+\pi^+)} < 4.6 \times 10^{-3} \tag{7.2}$$

which gives an absolute branching ratio of

$$BR(D^+ \to K^+\pi^0) < 4.2 \times 10^{-4}. \tag{7.3}$$

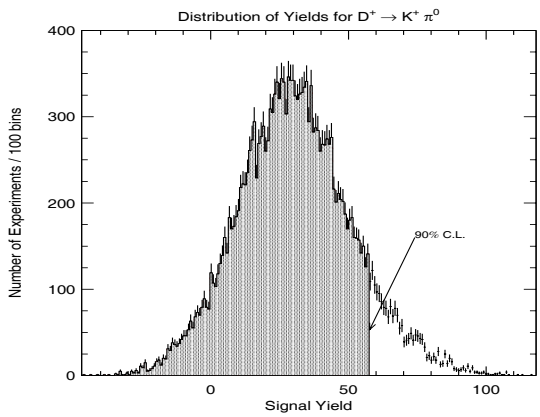

Figure 7.1: Distribution of $D^+ \to K^+\pi^0$ Signal Yields - 90% C.L. at 57.20

CHAPTER 8

Results of $SU(3)_F$ Breaking and Isospin Calculations

As discussed in Sec. 2.3, the results from this analysis are useful for testing $SU(3)_F$ predictions. To look directly at $SU(3)_F$ breaking effects, we observe decays of the D^+ which have the same contributing amplitudes (See Table 8.1) but differ by the existence of s quarks rather than d quarks. It may also be useful to look at decays with different contributing amplitudes, since this will shed light onto some of the dynamical assumptions made by the quark-diagram scheme. This chapter presents some calculations that are useful for studying $SU(3)_F$. The isospin amplitudes are also presented for the $K, D, B \to \pi\pi$ systems.

Decay Mode	Amplitudes
$D^+ \to \pi^+\pi^0$	$\sqrt{\frac{1}{2}}(s_1c_1)(a+b)$
π^+K_s	$(c_1)^2(a+b)$
$D^+ \to K^+\pi^0$	$\sqrt{\frac{1}{2}}(s_1)^2(a-d)$
K^+K_s	$(s_1c_1)(a-d)$

Table 8.1: Amplitudes from the quark-diagram scheme that contribute to the decay modes (see Figure 2.1). s_1 and c_1 refer to Cabibbo-suppressed and favored transitions, respectively. a is the external W-emission diagram, b is the internal W-emission diagram, and d is the W-annihilation diagram. The factor of $\sqrt{\frac{1}{2}}$ arises from the normalization condition on the π^0.

8.1 $SU(3)_F$ Symmetry Breaking

A ratio that is expected to be unity in the limit of $SU(3)_F$[36] is given by

$$R_1 = 2 \times \left|\frac{V_{cs}}{V_{cd}}\right|^2 \frac{\Gamma(D^+ \to \pi^+\pi^0)}{\Gamma(D^+ \to \bar{K}^0\pi^+)} \tag{8.1}$$

where V_{cs} and V_{cd} arise because of different quark transitions in the two decays and the factor of 2 arises because of the $\sqrt{\frac{1}{2}}$ term in the normalization of the π^0. This ratio is predicted to be unity because both decays only have contributions from the external and internal W-emission diagrams. Note that the W-annihilation term for $D^+ \to \pi^+\pi^0$ cancels because there is an amplitude from a $u\bar{u}$ and a $d\bar{d}$ pair being produced. Since the π^0 is defined as $\sqrt{\frac{1}{2}}(u\bar{u} - d\bar{d})$, these two amplitudes negate each other.

Using values from the PDG[2], we can obtain the following ratio:

$$\left|\frac{V_{cs}}{V_{cd}}\right|^2 = |\frac{0.996 \pm 0.013}{0.224 \pm 0.016}|^2 = 19.767 \pm 2.872. \tag{8.2}$$

Rewriting Eq. 8.1 and using our results from this analysis as well as Eq. 8.2, the ratio for R_1 becomes

$$R_1 = \left|\frac{V_{cs}}{V_{cd}}\right|^2 \frac{\Gamma(D^+ \to \pi^+\pi^0)}{\Gamma(D^+ \to K_s\pi^+)} = 1.267 \pm 0.247 \tag{8.3}$$

which is consistent with the $SU(3)_F$ prediction of unity.

A similar study can give us estimates on the number of events in our sample that are expected to contain the DCSD mode $D^+ \to K^+\pi^0$. This decay has the same diagram contributions as $D^+ \to \bar{K}^0K^+$. If we assume $SU(3)_F$ symmetry, then we can write the overall raw yield of the DCSD mode as

$$Yield(D^+ \to K^+\pi^0) \;=\; \left|\frac{V_{cd}}{V_{cs}}\right|^2 \frac{\epsilon_{K^+\pi^0}}{\epsilon_{K_SK^+}} Yield(D^+ \to K_SK^+) \tag{8.4}$$

$$= (0.0506)(\frac{0.0608}{0.0344})(277.70)$$
$$= 25.$$

The estimated yield of 25 events in the entire CLEO II and II.V sample, with an associated error of 30%, is very consistent with our result of 34.31 ± 20.88 events.

Dynamical assumptions are often used when applying the quark-diagram scheme to SU(3) studies and to make physical interpretations. For example, it is believed that a destructive interference between the external and internal W-exchange diagrams could be responsible for the difference in lifetimes between the D^+ and the D^0[37]. The BRs calculated in this analysis may also be used to study this destructive interference term by calculating the following ratios:

$$R_2 = \left|\frac{V_{cs}}{V_{cd}}\right|^2 \frac{\Gamma(D^+ \to \bar{K}^0 K^+)}{\Gamma(D^+ \to \bar{K}^0 \pi^+)} \tag{8.5}$$

and

$$R_3 = \frac{1}{2} \times \frac{\Gamma(D^+ \to \bar{K}^0 K^+)}{\Gamma(D^+ \to \pi^+ \pi^+)}. \tag{8.6}$$

Note that I am also making a dynamical assumption with the interpretation of these ratios. The decay $D^+ \to \bar{K}^0 K^+$ has two contributing diagrams: an external W-emission and an annihilation term. It has been argued[38] that the latter is negligible compared to the former, and therefore can be ignored. There are others, however, who argue that it may not be as negligible as previously believed[39]. For this discussion, I assume it is negligible; this gives a decay with an external W-emission in the numerator of R_2 and R_3 and both the external and internal W-emission diagrams in the denominator. Since the denominators have two contributing amplitudes, it is possible for them to interfere; the nature of the interference term will affect the ratios. If there were no interference, then we would expect these ratios to be unity.

A positive (constructive) interference would increase the size of the denominator, making these ratios less than unity; a negative (destructive) interference would decrease the size or the denominator, making these ratios greater than unity.

Since we are measuring $D^+ \to K_s\pi^+$ rather than $D^+ \to \bar{K}^0\pi^+$, we will use the commonly accepted relation that $BR(D^+ \to \bar{K}^0\pi^+) = 2 \times BR(D^+ \to K_s\pi^+)$. We note that it has been predicted[40] that interference between the CFD $BR(D^+ \to \bar{K}^0\pi^+)$ with the DCSD mode $D^+ \to K^0\pi^+$ (which are both valid decays for $D^+ \to K_s\pi^+$) could invalidate this assumption.

We use the same relation between K_S and $\bar{K}^0$ to rewrite Eqs. 8.5 and 8.6:

$$R_2 = \left|\frac{V_{cs}}{V_{cd}}\right|^2 \frac{\Gamma(D^+ \to K_sK^+)}{\Gamma(D^+ \to K_s\pi^+)} = 3.704 \pm 0.617 \tag{8.7}$$

and

$$R_3 = \frac{\Gamma(D^+ \to K_sK^+)}{\Gamma(D^+ \to \pi^0\pi^+)} = 2.922 \pm 0.435. \tag{8.8}$$

Given that they are both significantly larger than unity, we may conclude that the interference between external and internal diagrams must be destructive (or conclude that the effects of the annihilation term are extremely large). As expected from our result from Eq. 8.3, the values for R_2 and R_3 are consistent up to 1 σ.

8.1.1 Isospin

It is useful to decompose the decays of $K, D \to \pi\pi$ systems in terms of their isospin amplitudes. From Sec. 2.3.2, there are two isospin amplitudes for a spinless particle decaying into two πs: A_2 and A_0, where the former refers to the $\pi\pi$ final isospin state of $I = 2$ and the latter refers to the final state $I = 0$. Since we are using the measurements of BR, we may only calculate the absolute values of these

isospin amplitudes: $|\frac{A_2}{A_0}|$. By also calculating the relative phase between A_2 and A_0, however, we obtain full information regarding the isospin amplitudes.

This section begins with the introduction of some isospin formalism, which is derived in Appendix B. The ratio $|\frac{A_2}{A_0}|$ can be written in terms of the following decay widths: $\Gamma^{+-} = \frac{BR(X^0 \to \pi^+\pi^-)}{\tau_{X^0}}$, $\Gamma^{00} = \frac{BR(X^0 \to \pi^0\pi^0)}{\tau_{X^0}}$, and $\Gamma^{+0} = \frac{BR(X^+ \to \pi^+\pi^0)}{\tau_{X^+}}$, where X refers to the K or D mesons. This gives us

$$\left|\frac{A_2}{A_0}\right|^2 = \frac{\Gamma^{+0}}{\frac{3}{2}(\Gamma^{+-} + \Gamma^{00}) - \Gamma^{+0}} \tag{8.9}$$

and a phase difference of

$$cos\ \delta = \frac{3\Gamma^{+-} - 6\Gamma^{00} + 2\Gamma^{+0}}{4\sqrt{2\Gamma^{+0}}\sqrt{\frac{3}{2}(\Gamma^{+-} + \Gamma^{00}) - \Gamma^{+0}}}. \tag{8.10}$$

From Eqs. 8.9 and 8.10, we may calculate $|\frac{A_2}{A_0}|$ using our measurement of $D^+ \to \pi^+\pi^0$, combined with the PDG values for $D^0 \to \pi^0\pi^0, \pi^+\pi^-$. For comparison, we also calculate these values for the $K \to \pi\pi$ system using measurements from the PDG[2]. Table 8.2 indicates that there is a high suppression in the K system and a moderate suppression in the D system. To date, a good explanation still does not exist why there is such high suppression in the K system compared to the D system[41]. The result of the phase difference for the $D \to \pi\pi$ system shows $\delta = 88°$, indicating a large influence of FSI on this system. [42]

Decay	$\lvert\frac{A_2}{A_0}\rvert$	$cos\delta$
K	0.0451 ± 0.0003	0.471 ± 0.048
D	0.421 ± 0.044	0.042 ± 0.195

Table 8.2: Isospin amplitudes for $K, D \to \pi\pi$

8.2 Summary

Our results from $D^+ \to \pi^+\pi^0$ and $D^+ \to K_S\pi^+$ show good agreement with the predictions of $SU(3)_F$. This should allow better constraints to be put on the mixing parameters x and y, which are expected to be generated at the second order in $SU(3)_F$.

Using $SU(3)_F$ arguments and the mode $D^+ \to K_S K^+$, we also determined that the number of events obtained for our DCSD mode $D^+ \to K^+\pi^0$ is expected. The upper limit determined for this mode will also be useful in determining limits on mixing, since the corresponding DCSD mode for D^0 creates the interference term necessary to measure D-mixing.

By comparing our decays containing a external and internal W-emission diagram $(\pi^+\pi 0, K_S\pi^+)$ with one containing primarily an external W-emission term $(K_S K^+)$, we were able to show that there is a significant destructive interference between the external and internal W-emission diagrams. Understanding the dynamics of the quark-diagrams is necessary in order to apply this scheme to $SU(3)_F$ and D-mixing studies.

The results from the isospin study reveal some suppression in the $D \to \pi\pi$ system, but significantly less than in the $K \to \pi\pi$ system. Whereas a good explanation does not exist to describe this observation, the measurement of the large phase difference between the isospin modes shows the effects of FSI on this system. We expect large amounts of FSI because the mass of the D is close to the mass of many other resonant states, allowing for transitions via the strong interaction to proceed.

APPENDIX A

Glossary of Terms

amplitude: A term which corresponds to probability of a particle or system being an a particular state. E.g. the square of a "decay amplitude" gives the probability that a particle will *decay* into the particular state.

barn: A unit of area equal to 10^{-24} cm^2. An fb refers to a femto-barn, which consists of 10^{-12} barns.

CP violation: CP refers to the operations of "*C*harge-conjugation" and "*P*arity"; when combined, they transform a particle to its anti-particle. The violation of CP could help to explain the abundance of matter over anti-matter in the universe.

gauge symmetry: Refers to an invariance of physical laws under certain local transformations, which give rise to the force fields.

hadron: Any bound state of quarks. This encompasses mesons and baryons.

helicity: Refers to the spin component in the direction of motion. A particle is said to have "positive" helicity if its spin state is parallel to the direction of motion and "negative" if it is anti-parallel to the direction of motion. If a particle is massless, a negative helicity state is equivalent to a "left-handed" state, and a positive helicity state is equivalent to a "right-handed" state.

perturbation theory: With respect to calculations of forces, it involves starting with the initial assumption that particles do not interact to determine a rough approximation. Improvements to the calculation are obtained by adding successive terms describing the interaction. This only works for if the interaction terms are small; this is not the case for the strong interaction since it grows with respect to the separation distance of strongly-interacting particles.

spin: An inherent property of every particle, which corresponds to an intrinsic value of angular momentum. Particles with integer spin are called "bosons" and those with half-integer spin are called "fermions".

APPENDIX B

Isospin Formalism

The π mesons form an isotriplet state of I=1. The state vectors ($|I, I_3\rangle$) are given as

$$\begin{aligned} \left|\pi^+\right\rangle &= |1,1\rangle \\ \left|\pi^0\right\rangle &= |1,0\rangle \\ \left|\pi^-\right\rangle &= |1,-1\rangle \end{aligned} \tag{B.1}$$

The isospin state vectors for the $\pi\pi$ final states can then be generically written as

$$\begin{aligned} \left|\pi^+\pi^-\right\rangle &= \alpha_2 |2,0\rangle + \beta_2 |1,0\rangle + \delta_2 |0,0\rangle \\ \left|\pi^0\pi^0\right\rangle &= \alpha_3 |2,0\rangle + \beta_3 |1,0\rangle + \delta_3 |0,0\rangle \\ \left|\pi^+\pi^0\right\rangle &= \alpha_1 |2,1\rangle + \beta_1 |1,1\rangle \end{aligned} \tag{B.2}$$

For identical bosons, the overall wave function must be symmetric. With respect to the strong force, all πs are considered identical, so we expect the TOTAL wave function to be symmetric.

Since D^+ is a spin-0 particle, the wavefunction for angular momentum for $|\pi\pi\rangle$ is symmetric. This means that the wave function for isospin must also be symmetric. The contribution from I=1 is anti-symmetric in nature, so we ignore these

terms. Using this symmetry argument with the Clebsh-Gordon coefficients, Eqs. B.2 become

$$\begin{aligned}
\left|\pi^+\pi^-\right\rangle &= \sqrt{\frac{1}{3}}\,|2,0\rangle + \sqrt{\frac{2}{3}}\,|0,0\rangle \\
\left|\pi^0\pi^0\right\rangle &= \sqrt{\frac{2}{3}}\,|2,0\rangle - \sqrt{\frac{1}{3}}\,|0,0\rangle \\
\left|\pi^+\pi^0\right\rangle &= |2,1\rangle
\end{aligned} \tag{B.3}$$

To determine the amplitude of a D meson decaying into a $\pi\pi$, we need to separate (or "decompose") the interaction hamiltonian H into an isospin-invariant interaction hamiltonian h, and an isospin-changing term S. The latter is called a "spurion", which is a fictitous particle, possessing neither energy nor momentum[43]. S is defined as the normalized superposition of all state vectors that will conserve I and I_3 between the initial and final states.

For our modes, S will include a term for $I = \frac{1}{2}$ and $I = \frac{3}{2}$ since the isospin of the D is $\frac{1}{2}$ and a $\pi\pi$ final state allows for $I = 0, 1, 2$. The $|S\rangle\,|D\rangle$ states for our decay are then defined by

$$|S_1\rangle\left|D^0\right\rangle = \left[\frac{1}{N_1}\left(\left|\frac{1}{2},\frac{1}{2}\right\rangle + \left|\frac{3}{2},\frac{1}{2}\right\rangle\right)\right]\left|\frac{1}{2},-\frac{1}{2}\right\rangle = \frac{1}{\sqrt{2}}(|2,0\rangle + |0,0\rangle) \tag{B.4}$$

$$|S_2\rangle\left|D^+\right\rangle = \left[\frac{1}{N_2}\left(\left|\frac{1}{2},\frac{1}{2}\right\rangle + \left|\frac{3}{2},\frac{1}{2}\right\rangle\right)\right]\left|\frac{1}{2},\frac{1}{2}\right\rangle = \frac{\sqrt{3}}{2}\,|2,1\rangle + \frac{1}{2}\,|1,1\rangle) \tag{B.5}$$

where N_1 and N_2 are normalization factors for the state vectors. Again note that we ignore contributions from anti-symmetric states.

We can define the following isospin amplitudes:

$$A_0 = \frac{1}{\sqrt{2}}\,\langle 0,0|h|0,0\rangle \tag{B.6}$$

$$A_2 = \frac{1}{\sqrt{2}}\,\langle 2,0|h|2,0\rangle \tag{B.7}$$

where A_0 represents the $\Delta I = \frac{1}{2}$ transition and A_2 represents the $\Delta I = \frac{3}{2}$ transition. Taking advantage of the Wigner-Eckart theorem to set $\langle 2,1|h|2,1\rangle = \langle 2,0|h|2,0\rangle$, the following relations are obtained for the decay amplitudes from Eqs. B.3, B.4, and B.5

$$\begin{aligned} A^{+-} &= \sqrt{\frac{1}{3}}A_2 + \sqrt{\frac{2}{3}}A_0 \\ A^{00} &= \sqrt{\frac{2}{3}}A_2 - \sqrt{\frac{1}{3}}A_0 \\ A^{+0} &= \sqrt{\frac{3}{2}}A_2 \end{aligned} \tag{B.8}$$

where the superscripts reflect the charge of the $\pi\pi$ final state.

From this point, we need to extract $|\frac{A_2}{A_0}|^2$ and $\cos\delta$, where δ is the relative phase between A_2 and A_0. To derive the former, we take Eq.B.8 and rewrite A_0 in terms of A^{+-} and A^{00}.

$$\begin{aligned} A_0 &= \sqrt{\frac{2}{3}}A^{+-} - \sqrt{\frac{1}{3}}A^{00} \\ |A_0|^2 &= \frac{2}{3}|A^{+-}|^2 + \frac{1}{3}|A^{00}|^2 - \frac{2\sqrt{2}}{3}A^{+-}\cdot A^{00}. \end{aligned} \tag{B.9}$$

We then solve for $A^{+-}\cdot A^{00}$ using A^{+0}

$$\begin{aligned} A^{+0} &= \sqrt{\frac{3}{2}}A_2 = \sqrt{\frac{1}{2}}A^{+-} + A^{00} \\ |A^{+0}|^2 &= \frac{1}{2}|A^{+-}|^2 + |A^{00}|^2 + \sqrt{2}A^{+-}\cdot A^{00} \\ A^{+-}\cdot A^{00} &= \sqrt{\frac{1}{2}}|A^{+0}|^2 - \frac{1}{2\sqrt{2}}|A^{+-}|^2 - \sqrt{\frac{1}{2}}|A^{00}|^2 \end{aligned} \tag{B.10}$$

and substitute this into Eq. B.9

$$|A_0|^2 = |A^{+-}|^2 + |A^{00}|^2 - \frac{2}{3}|A^{+0}|^2. \tag{B.11}$$

Using $A_2 = \sqrt{\frac{2}{3}}A^{+0}$ and Eq. B.11,

$$|\frac{A_2}{A_0}|^2 = \frac{|A^{+0}|^2}{\frac{3}{2}(|A^{+-}|^2 + |A^{00}|^2) - |A^{+0}|^2}. \tag{B.12}$$

Since $\Gamma^{ij} = |A^{ij}|^2$,

$$|\frac{A_2}{A_0}|^2 = \frac{\Gamma^{+0}}{\frac{3}{2}(\Gamma^{+-} + \Gamma^{00}) - \Gamma^{+0}} \tag{B.13}$$

For cosδ, we use the dot product rule, which states

$$A_0 \cdot A_2 = |A_0||A_2|cos\delta. \tag{B.14}$$

Using Eq. B.8, we rewrite A_0 and A_2 in terms of A^{+-} and A^{00} and dot them into each other.

$$\begin{aligned} A_2 &= \sqrt{\frac{1}{3}}A^{+-} + \sqrt{\frac{2}{3}}A^{00} \\ A_0 &= \sqrt{\frac{2}{3}}A^{+-} - \sqrt{\frac{1}{3}}A^{00} \\ A_0 \cdot A_2 &= \frac{\sqrt{2}}{3}|A^{+-}|^2 - \frac{\sqrt{2}}{3}|A^{00}|^2 + \frac{1}{3}A^{+-} \cdot A^{00} \end{aligned} \tag{B.15}$$

Substituting Eq. B.10 into Eq. B.15, we get

$$A_0 \cdot A_2 = \frac{3}{6\sqrt{2}}|A^{+-}|^2 - \frac{6}{6\sqrt{2}}|A^{00}|^2 + \frac{2}{6\sqrt{2}}|A^{+0}|^2 \tag{B.16}$$

which can be simplified to

$$A_0 \cdot A_2 = (\frac{1}{6\sqrt{2}})(3\Gamma^{+-} - 6\Gamma^{00} + 2\Gamma^{+0}). \tag{B.17}$$

Using the previously determined values for $|A_2|$ and $|A_0|$, we can now solve Eq. B.14. The result is

$$cos\delta = \frac{3\Gamma^{+-} - 6\Gamma^{00} + 2\Gamma^{+0}}{4\sqrt{2\Gamma^{+0}}\sqrt{\frac{3}{2}(\Gamma^{+-} + \Gamma^{00}) - \Gamma^{+0}}} \tag{B.18}$$

APPENDIX C

Consistency Check – Cut Analysis

The cut analysis is the most straightforward way of determining a branching ratio; it involves choosing a single variable to fit (in our case, it was the mass of the reconstructed D^+), and cutting on all other variables to create the best possible $\frac{S}{\sqrt{B}}$ for the fitted variable. The cut analysis was done for all of the signal modes as a means of cross-checking the results returned from the fitter analysis; therefore, I did not go to great lengths to optimize cuts or efficiencies as was done for the fitter analysis. Also, no systematics were calculated.

C.1 Event Selection for Cut Analysis

The same cuts were used for general track quality and π^0 selection as in the fitter analysis (See Ch. 4). The 5 σ cut on the D^+ mass as in the fitter analysis. The cuts listed below have been optimized to return the best $\frac{S^2}{B}$.

- mass difference between D^* and $D < 2\sigma$
- $x_{p_{D*}} > 0.65$
- $|cos\theta_{helicity}| < 0.8$

- Particle ID Cuts:
  - $|SGKADI(K)| < 2.0$
  - $|SGPIDI(\pi)| < 3.0$

C.2 Efficiency Calculation

To calculate efficiency, we generated large samples of signal Monte Carlo for each mode. We then ran each sample through our cuts and fit the D^+ mass distribution to a bifurcated Gaussian and a second order polynomial. The resulting efficiencies are listed in Table C.1.

Dataset	Mode	Input Events	Signal Yield	TOTAL ϵ
CLEO II	$\pi^+\pi^0$	20000	934.78 ± 39.54	$(4.67 \pm 0.20)\%$
	$K^+\pi^0$	28037	1335.7 ± 45.55	$(4.76 \pm 0.16)\%$
	$K^-\pi^+\pi^+$	60000	2834.3 ± 99.04	$(4.72 \pm 0.17)\%$
CLEO II.V	$\pi^+\pi^0$	59239	2898.7 ± 62.53	$(4.89 \pm 0.11)\%$
	$K^+\pi^0$	48860	2254.6 ± 56.76	$(4.61 \pm 0.12)\%$
	$K^-\pi^+\pi^+$	122593	6145.8 ± 113.35	$(5.01 \pm 0.09)\%$
CLEO II & II.V	$\pi^+\pi^0$	79239	3863.2 ± 73.10	$(4.88 \pm 0.09)\%$
	$K^+\pi^0$	76897	3585.6 ± 71.20	$(4.66 \pm 0.09)\%$
	$K^-\pi^+\pi^+$	182593	8970.1 ± 149.09	$(4.91 \pm 0.08)\%$

Table C.1: Reconstruction Efficiencies from CLEO II and II.V MC

C.3 Results

After our MC study, we ran over the entire CLEO II and II.V data sets. The resulting raw yields are given in Table C.2. Using the efficiencies from Table C.1 we obtain the following ratio of branching ratios:

$$\frac{BR(D^+ \to \pi^+\pi^0)}{BR(D^+ \to K^-\pi^+\pi^+)} = 0.0129 \pm 0.0027 \tag{C.1}$$

$$\frac{BR(D^+ \to K^+\pi^0)}{BR(D^+ \to K^-\pi^+\pi^+)} = 0.0018 \pm 0.0023 \tag{C.2}$$

Mode	Yield
$\pi^+\pi^0$	127.56 ± 26.92
$K^+\pi^0$	16.57 ± 21.87
$K^-\pi^+\pi^+$	9949.4 ± 156.24

Table C.2: Yields from CLEO II and II.V data

For $D^+ \to K^+\pi^-\pi^-$, it was necessary to allow the mean of the mass plot to float because there is a small shift from MC and data.

Our result for $D^+ \to \pi^+\pi^0$ differs significantly from the previous CLEO result[22]. We therefore went through consistency checks to see if we could account for this discrepancy. These checks included reproducing the previous result[22] and looking at CLEO II and II.V separately.

C.3.1 Consistency Checks for $D^+ \to \pi^+\pi^0$

C.3.2 Reproducing CBX 92-111

The measurement of $D^+ \to \pi^+\pi^0$ had been done by CLEO in 1992 using the 4s2 and 4s3 precompress data[22]. The result obtained by this measurement was

$$\frac{B(D^+ \to \pi^+\pi^0)}{B(D^+ \to K^-\pi^+\pi^+)} = 0.028 \pm 0.006 \pm 0.005 \tag{C.3}$$

MINUIT χ^2 Fit to Plot 1&0
skim. dmass axis
File: Generated internally 7-JAN-2003 10:16
Plot Area Total/Fit 744.00 / 744.00 Fit Status 3
Func Area Total/Fit 701.74 / 701.74 E.D.M. 6.777E-13
χ^2= 42.3 for 50 - 4 d.o.f., C.L.= 62.9%

Errors			Parabolic		Minos		
Function 1: Bifurcated Gaussian (sigma)							
AREA	127.56	±	26.92	-	26.90	+	26.90
* MEAN	1.8711	±	0.0000E+00	-	0.0000E+00	+	0.0000E+00
* SIGA	2.16410E-02	±	0.0000E+00	-	0.0000E+00	+	0.0000E+00
* SIGB	1.45899E-02	±	0.0000E+00	-	0.0000E+00	+	0.0000E+00
Function 2: Chebyshev Polynomial of Order 2							
NORM	2910.2	±	150.0	-	150.0	+	150.0
CHEB01	-0.27957	±	7.1200E-02	-	7.1046E-02	+	7.1346E-02
CHEB02	4.05112E-02	±	9.7820E-02	-	9.8202E-02	+	9.7614E-02

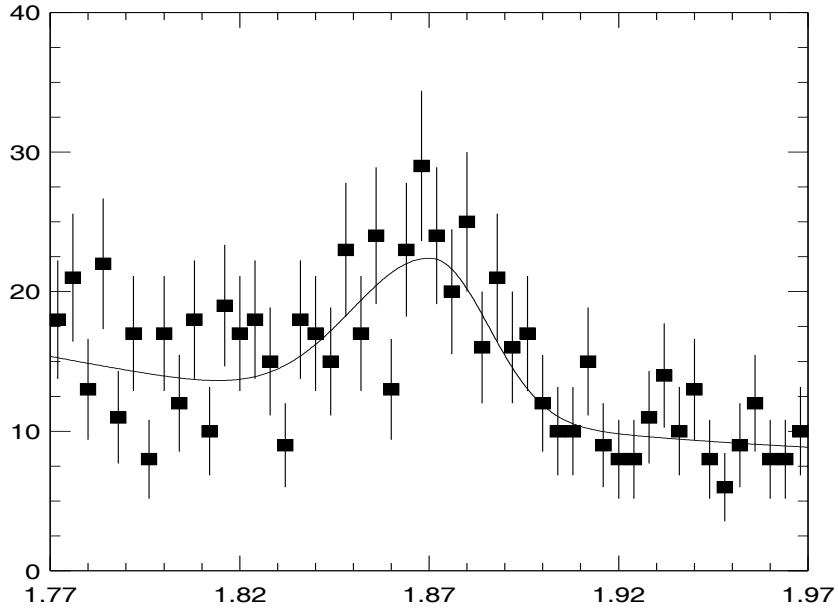

Figure C.1: Data Yield for $D^+ \to \pi^+\pi^0$ using 4s2 - 4sT

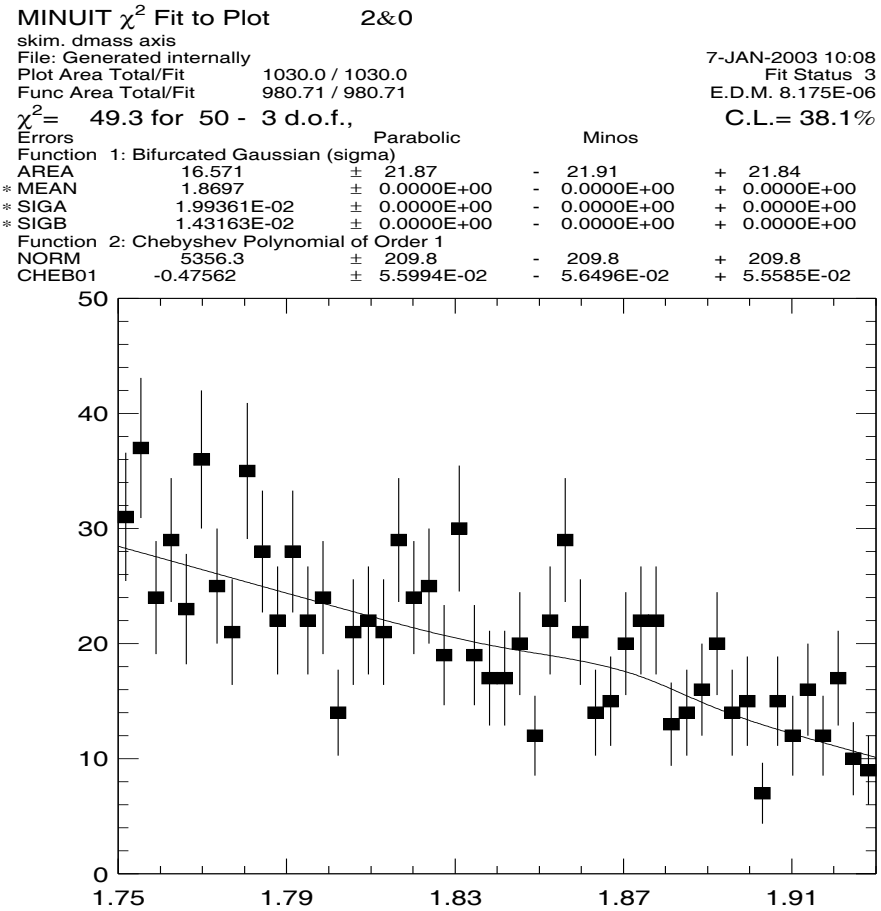

Figure C.2: Data Yield for $D^+ \to K^+\pi^0$ using 4s2 - 4sT

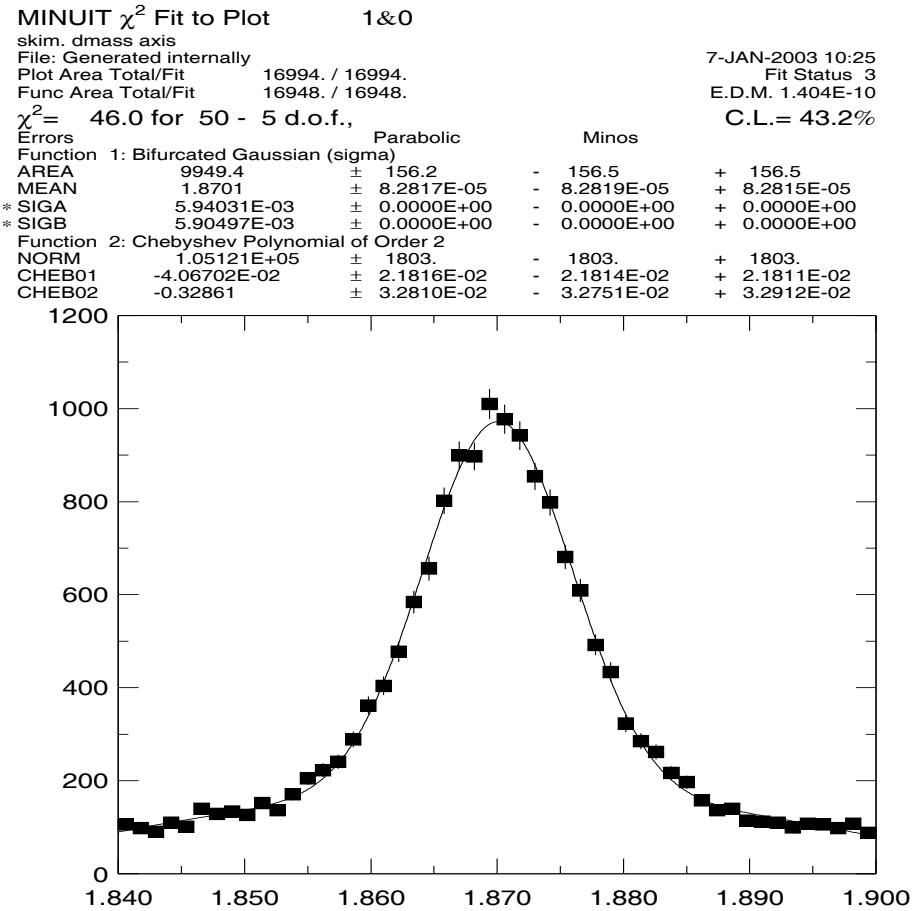

Figure C.3: Data Yield for $D^+ \to K^-\pi^+\pi^+$ using 4s2 - 4sT

Using our optimal cuts from the MC study, we obtained the following yields from the 4s2 and 4s3 data sets:

Mode	Yield	Efficiency
$\pi^+\pi^0$	26.55 ± 7.54	0.0386 ± 0.0011
$K^-\pi^+\pi^+$	720.07 ± 33.02	0.0304 ± 0.0005

Table C.3: Yields from 4s2 and 4s3 data sets

Our resulting branching fraction is

$$\frac{B(D^+ \to \pi^+\pi^0)}{B(D^+ \to K^-\pi^+\pi^+)} = 0.029 \pm 0.008 \tag{C.4}$$

which gave us confidence that we were not doing something out of the ordinary.

C.3.3 Looking at CLEO II and II.V independently

We wanted to check to see if there were differences between measuring branching fractions using CLEO II vs. II.V data. Using the MC, we determined that although the sigma for the D^+ mass plot differs between CLEO II and II.V, their efficiencies are not only consistent with each other, but also with value of the overall efficiency. We therefore use the same values from Table C.1. Our yields and resulting branching fractions are listed as follows:

MINUIT χ^2 Fit to Plot 1&0

Ds. dmass axis

File: Generated internally 1-MAY-2002 16:25

Plot Area Total/Fit 53.000 / 53.000 Fit Status 3

Func Area Total/Fit 44.706 / 44.706 E.D.M. 1.104E-06

χ^2= 10.0 for 20 - 4 d.o.f., C.L.= 86.7%

Errors			Parabolic		Minos		
Function 1: Bifurcated Gaussian (sigma)							
AREA	26.554	±	7.538	-	0.0000E+00	+	0.0000E+00
* MEAN	1.8692	±	0.0000E+00	-	0.0000E+00	+	0.0000E+00
* SIGA	2.03081E-02	±	0.0000E+00	-	0.0000E+00	+	0.0000E+00
* SIGB	1.57310E-02	±	0.0000E+00	-	0.0000E+00	+	0.0000E+00
Function 2: Chebyshev Polynomial of Order 2							
NORM	138.96	±	37.40	-	0.0000E+00	+	0.0000E+00
CHEB01	-0.80048	±	0.3832	-	0.0000E+00	+	0.0000E+00
CHEB02	1.0404	±	0.5283	-	0.0000E+00	+	0.0000E+00

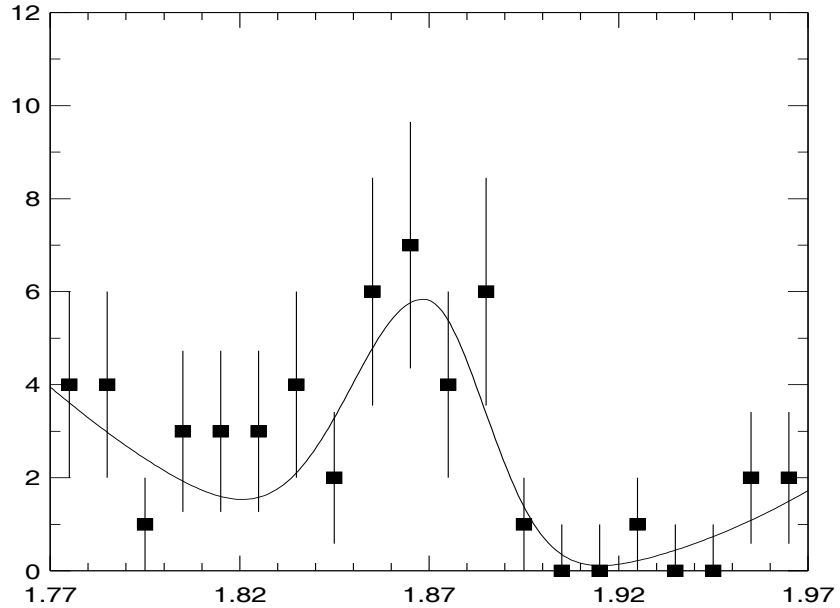

Figure C.4: Data Yield for $D^+ \to \pi^+\pi^0$ using 4s2 4s3

MINUIT χ^2 Fit to Plot 2&0

Ds. dmass axis

File: Generated internally 1-MAY-2002 16:29

Plot Area Total/Fit 1093.0 / 1093.0 Fit Status 3

Func Area Total/Fit 975.44 / 975.44 E.D.M. 6.475E-07

χ^2= 122.8 for 60 - 3 d.o.f., C.L.=0.101E-03%

Errors			Parabolic		Minos		
Function 1: Sum Two Bifurcated Gaussians (sigma							
AREA	720.07	±	33.02	-	0.0000E+00	+	0.0000E+00
* MEAN	1.8699	±	0.0000E+00	-	0.0000E+00	+	0.0000E+00
* SIGA1	5.48313E-03	±	0.0000E+00	-	0.0000E+00	+	0.0000E+00
* SIGB/SIGA	0.95032	±	0.0000E+00	-	0.0000E+00	+	0.0000E+00
* AR2/AREA	0.36423	±	0.0000E+00	-	0.0000E+00	+	0.0000E+00
* SIG2/SIG1	1.9345	±	0.0000E+00	-	0.0000E+00	+	0.0000E+00
Function 2: Chebyshev Polynomial of Order 1							
NORM	4273.1	±	421.1	-	0.0000E+00	+	0.0000E+00
CHEB01	-0.11360	±	0.1233	-	0.0000E+00	+	0.0000E+00

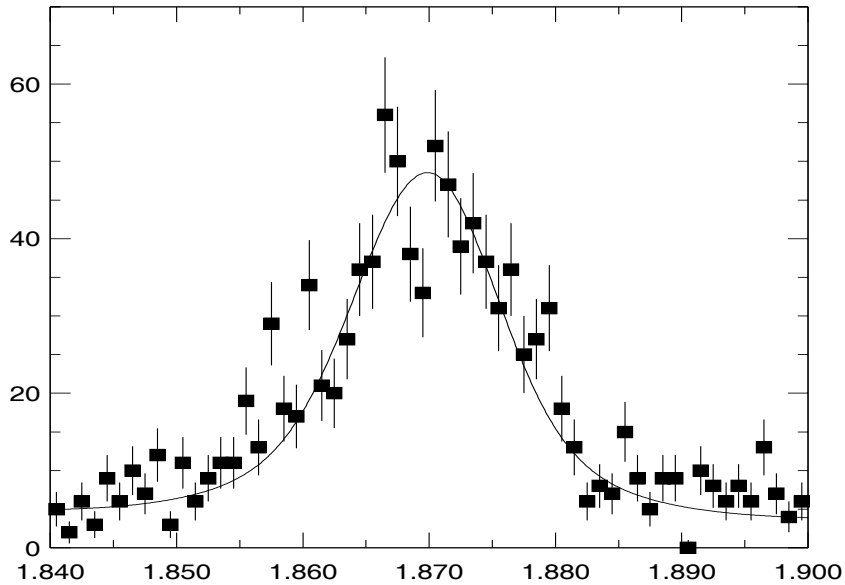

Figure C.5: Data Yield for $D^+ \to K^-\pi^+\pi^+$ using 4s2 and 4s3

Dataset	Mode	Yield	Normalized BR
CLEO II	$\pi^+\pi^0$	67.24 ± 12.35	0.0190 ± 0.0035
	$K^-\pi^+\pi^+$	3139.1 ± 64.2	
CLEO II.V	$\pi^+\pi^0$	86.78 ± 14.62	0.0125 ± 0.0021
	$K^-\pi^+\pi^+$	6174.9 ± 86.32	

Table C.4: Yields from CLEO II and II.V data sets.

BIBLIOGRAPHY

[1] D. Griffiths, *Introduction to Elementary Particles* (John Wiley & Sons, Inc., New York, 1987).

[2] K. Hagiwara *et al.*, *Review of particle physics*, Phys. Rev. **D66**, 010001 (2002).

[3] J. F. Donoghue, E. Golowich, and B. R. Holstein, *Dynamics of the Standard Model* (Cambridge University Press, Cambridge, 1992).

[4] B. Greene, *The Elegant Universe* (W. W. Norton & Company, New York, NY, 1999).

[5] L. H. Ryder, *Quantum Field Theory – 2nd Edition* (Cambridge University Press, Great Britain, 1996).

[6] L. Lederman and D. Teresi, *The God Particle* (Delta Publishing, New York, NY, 1993).

[7] T. Kajita, *Atmospheric neutrino results from Super-Kamiokande and Kamiokande: Evidence for nu/mu oscillations*, Nucl. Phys. Proc. Suppl. **77**, 123 (1999).

[8] N. Cabibbo, *UNITARY SYMMETRY AND LEPTONIC DECAYS*, Phys. Rev. Lett. **10**, 531 (1963).

[9] D. Perkins, *Introduction to High Energy Physics* (Cambridge University Press, Great Britain, 2000).

[10] S. L. Glashow, J. Iliopoulos, and L. Maiani, *WEAK INTERACTIONS WITH LEPTON - HADRON SYMMETRY*, Phys. Rev. **D2**, 1285 (1970).

[11] M. Kobayashi and T. Maskawa, *CP violation in the renormalizable theory of weak interaction*, Prog. Theor. Phys. **49**, 652 (1973).

[12] J. D. Bjorken and S. L. Glashow, *ELEMENTARY PARTICLES AND SU(4)*, Phys. Lett. **11**, 255 (1964).

[13] L.-L. Chau and H.-Y. Cheng, *Analysis of exclusive two body decays of charm mesons using the quark diagram scheme*, Phys. Rev. **D36**, 137 (1987).

[14] F. Halzen and A. D. Martin, *Quarks & Leptons: An Introductory Course in Modern Particle Physics* (John Wiley & Sons, Inc., New York, 1984).

[15] A. F. Falk, Y. Grossman, Z. Ligeti, and A. A. Petrov, *SU(3) breaking and D0 - anti-D0 mixing*, Phys. Rev. **D65**, 054034 (2002).

[16] A. Petrov, *private communication.*

[17] R. E. Marshak, Riazuddin, and C. P. Ryan, *Theory of Weak Interactions* (Wiley-Interscience, New York, 1969).

[18] M. Sands, *The Physics of Electron Storage Rings*, SLAC Note SLAC-121, (Internal Report).

[19] Y. Kubota *et al.*, *The CLEO-II Detector*, Nucl. Instrum. Meth. **A320**, 66 (1992).

[20] D. Jaffe, *Comprehensive QQ Documentation*, available in CLEO internal website.

[21] R. Brun *et al.*, *GEANT3 User's Guide*, CERN DD/EE/84-1, website.

[22] M. Selen *et al.*, *The D → pi pi branching fractions*, Phys. Rev. Lett. **71**, 1973 (1993).

[23] M. Bishai *et al.*, *Analyses of D+ → K0(S) K+ and D+ → K0(S) pi+*, Phys. Rev. Lett. **78**, 3261 (1997).

[24] L.-L. Chau and H.-Y. Cheng, *Predictions for the quark-mixing doubly suppressed decays of charmed mesons*, Phys. Rev. **D42**, 1837 (1990).

[25] G. Moneti, *private communication.*

[26] S. Roberts, L. Gibbons, and E. Thorndike, *Trkman the Next Generation: The quest for track quality*, CBX 96-103, (Internal Report).

[27] C. Prescott, *The KNVF Secondary Vertex Finding Package*, CSN 97/353, (Internal Report).

[28] L. Lyons, *Statistics for nuclear and particle physics* (Cambridge University Press, Great Britain, 1986).

[29] W. T. Ford, *Poisson likelihood fits and rare B branching fraction measurements*, CBX 98-6, (Internal Report).

[30] F. James, *MINUIT - Minimization package Reference Manual*, http://wwwinfo.cern.ch/asdoc/WWW/minuit/minmain/minmain.html.

[31] V. Savinov, *private communication.*

[32] G. Moneti, *Charm Fragmentation*, Charm pta talk, (Internal Report).

[33] T. Pedlar *et al.*, *Measurement of B- → D0 pi- and B0 → D+ pi- and Isospin Analysis of B → D pi Decays*, CBX 02-15, (Internal Report).

[34] J. Alexander *et al.*, *CLEO III Measurement of Rare Hadronic B Decays*, CBX 02-37, (Internal Report).

[35] J. M. Link *et al. Search for CP Violation in the decays* $D+ \to K_S pi+ and D+ \to K_S K+$, (unpublished).

[36] L.-L. Chau and H.-Y. Cheng, *SU(3) breaking effects in charmed meson decays*, Phys. Lett. **B333**, 514 (1994).

[37] J. F. Labs *Search for doubly Cabibbo suppressed decays of the charged D meson*, (unpublished).

[38] M. Lusignoli and A. Pugliese *A comment on hadronic charm decays*, (unpublished).

[39] H.-Y. Cheng, *Weak annihilation and the effective parameters a1 and a2 in nonleptonic D decays*, Eur. Phys. J. **C26**, 551 (2003).

[40] I. I. Y. Bigi and H. Yamamoto, *Interference between Cabibbo allowed and doubly forbidden transitions in D → K(S), K(L) + pi's decays*, Phys. Lett. **B349**, 363 (1995).

[41] H.-Y. Cheng, *private communication.*

[42] T. E. Browder, K. Honscheid, and D. Pedrini, *Nonleptonic decays and lifetimes of charm and beauty particles*, Ann. Rev. Nucl. Part. Sci. **46**, 395 (1996).

[43] L. Okun, *Leptons and Quarks* (North-Holland Personal Library, The Netherlands, 1982).